

# Fourth-order conservative non-splitting semi-Lagrangian Hermite WENO schemes for kinetic and fluid simulations

Nanyi Zheng<sup>a</sup>, Xiaofeng Cai<sup>b,c,\*</sup>, Jing-Mei Qiu<sup>d</sup>, Jianxian Qiu<sup>e</sup>

<sup>a</sup>*School of Mathematical Sciences, Xiamen University, Xiamen, Fujian 361005, China*

<sup>b</sup>*Research Center for Mathematics, Beijing Normal University, Zhuhai 519087, China*

<sup>c</sup>*BNU-HKBU United International College, Zhuhai 519087, China*

<sup>d</sup>*Department of Mathematical Sciences, University of Delaware, Newark, DE, 19716, USA*

<sup>e</sup>*School of Mathematical Sciences and Fujian Provincial Key Laboratory of Mathematical Modeling and High-Performance Scientific Computing, Xiamen University, Xiamen, Fujian 361005, China*

---

## Abstract

We present fourth-order conservative non-splitting semi-Lagrangian (SL) Hermite essentially non-oscillatory (HWENO) schemes for linear transport equations with applications for nonlinear problems including the Vlasov-Poisson system, the guiding center Vlasov model, and the incompressible Euler equations in the vorticity-stream function formulation. The proposed SL HWENO schemes combine a weak formulation of the characteristic Galerkin method with two newly constructed HWENO reconstruction methods. Fourth-order accuracy is accomplished in both space and time under a non-splitting setting. Mass conservation naturally holds due to the weak formulation of the characteristic Galerkin method and the design of the HWENO reconstructions. We apply a positive-preserving limiter to maintain the positivity of numerical solutions when needed. Although the proposed SL framework allows us to take large time steps for improving computational efficiency, it also brings challenges to the spatial reconstruction technique; we construct two kind of novel HWENO reconstructions to fit the need for the proposed SL framework. Abundant benchmark tests are performed to verify the effectiveness of the proposed SL HWENO schemes.

**Key Words: positivity preservation; non-splitting scheme; conservative semi-Lagrangian; HWENO reconstruction; Vlasov systems; incompressible flows.**

---

---

\*Corresponding authors

*Email addresses:* nyzheng@stu.xmu.edu.cn (Nanyi Zheng), xfcai@bnu.edu.cn (Xiaofeng Cai), jingqiu@udel.edu (Jing-Mei Qiu), jxqiu@xmu.edu.cn (Jianxian Qiu)

## 1. Introduction

Semi-Lagrangian (SL) schemes have been developed in areas of applications such as numerical weather prediction [35, 18, 3], kinetic description of plasma [13, 9, 31], and fluid simulations [25, 37]. Most SL schemes are designed to solve the transport equation in the form of

$$u_t + \nabla_{\mathbf{x}} \cdot (\mathbf{a}(u, \mathbf{x}, t)u) = 0, \quad (1.1)$$

where  $u(\mathbf{x}, t)$  usually represents a density function of a conservative quantity in a velocity field  $\mathbf{a}(u, \mathbf{x}, t)$  with  $\mathbf{x} \in \mathbb{R}^d$ . Comparing with the Eulerian and the Lagrangian approaches, the SL approach naturally holds its advantages in terms of accuracy and efficiency for certain applicable problems. On one hand, the same with the Lagrangian approach, the SL approach evaluates the solution along the convection characteristics. Hence, it allows large numerical time steps comparing with the Eulerian approach. On the other hand, as the Eulerian approach, the SL approach adopts a fixed spatial mesh equipped with a wide range of different solution spaces for high-order spatial accuracy. As a comparison, the Lagrangian approach suffers from statistical noises and only achieves a low order of  $O(1/\sqrt{N})$  with  $N$  representing the number of sampling points.

The geometry structure of transport dynamics can be very complicated. For instance, the Vlasov-Poisson system has drastic high-frequency filamentation structures [31, 29] and the guiding center Vlasov model has steep structures [36]. To handle such complicated structures, the SL approach has been successfully coupled with the discontinuous Galerkin (DG) method [30, 29, 22], the weighted essentially non-oscillatory (WENO) schemes [28, 19, 34], and the Hermite WENO (HWENO) schemes [38, 6, 41]. However, there are pros and cons for each type of spatial discretization. For the DG method, it needs many degrees of freedom (DOF) per element for its high-order version, especially in a high-dimensional setting. For high-order WENO schemes, they always require very wide reconstruction stencils, compared with the DG method. The HWENO methods can be regarded as an intermediate transition from the DG method to a WENO method. It requires significantly lower degrees of freedom per element compared with the DG method, and it uses a more compact stencil for high-order reconstruction compared with a WENO method.

The HWENO method was first introduced by Qiu and Shu in [26] and was further developed in [27, 7, 11, 40]. Notice that the HWENO schemes in [26, 27, 7, 11] use point-wise positive linear weights to present the information of a high-degree polynomial as a convex combination of

the information of several low-degree polynomials. In [26, 27, 7, 11], such positive linear weights do exist for the specific Gaussian points they require. However, one can find that such positive linear weights do not exist for some special locations (even regions) in an Eulerian grid for each HWENO reconstruction in [26, 27, 7, 11]. Notice that characteristic feet for (1.1) can be located anywhere on an Eulerian grid; and the reconstruction designs in [26, 27, 7, 11] are not suitable for an SL method. Based on the observation above, in our previous work [41], we adopted a 1-D hybrid HWENO reconstruction method proposed in [40], and developed a dimensional-splitting SL hybrid HWENO scheme. Although the numerical results of the splitting-based SL HWENO scheme are satisfying for most cases, we observe that the scheme is very dissipative for large-gradient extreme points. The reason for the dissipation problem is that both the troubled cell indicator and the HWENO reconstruction are not able to distinguish large-gradient extreme points from discontinuities. Hence, the hybrid HWENO reconstruction decays to a first-degree polynomial reconstruction near large-gradient extreme points.

To overcome the dissipation issue, we propose two new two-dimensional (2-D) HWENO reconstruction methods, denoted by HWENO-1 and HWENO-2. Comparing with the HWENO reconstruction technique in [40], a key difference of the newly constructed reconstructions is that we rule out the participation of any first-degree polynomial, which leads to large numerical dissipation. The two newly proposed HWENO methods gather information from central or one-sided constructed polynomials, which are at least quadratic. Theoretically, a good HWENO reconstruction approximates the highest-degree polynomial where the solution is continuous and reduces to a one-sided lower-degree polynomial when a discontinuity is involved. To achieve such a principle, we attempt two different strategies. For the HWENO-1, we follow the same technique in [40], but base on newly chosen polynomials. The resulting HWENO-1 method has a significant improvement in reducing numerical dissipation. On the other hand, the HWENO-2 directly selects one polynomial from all candidates. This is equivalent to assigning weights of one or zero to candidate polynomials. The stencil selection strategy of the HWENO-2 is motivated by the targeted essentially non-oscillatory (TENO) schemes developed by Fu et al. [16, 17, 15]. Recently, a Hermite TENO (HTENO) is developed in [20], which shows very good numerical results. There are two reasons not to apply the HTENO method proposed in [20]. Firstly, it depends on point-wise positive linear weights as we mentioned before. Secondly, it is only a one-dimensional version method. Both the

HWENO-1 and HWENO-2 have a huge improvement in terms of dissipation comparing with the HWENO reconstruction in [40]. But, there are subtle differences in effectiveness. On one hand, The HWENO-1 is “smoother” due to its nature of assigning non-zero weight to each candidate polynomial. As a comparison, the HWENO-2 (or HTENO) only chooses one candidate, which means the piecewise polynomial constructed by the HWENO-2 can be fragmented sometimes. On the other hand, The HWENO-2 is more robust for capturing discontinuity since the highest-degree polynomial is not involved at all as long as the stencil selecting strategy works correctly. In this paper, we will describe the construction of the HWENO-1 and HWENO-2 in details and compare these two strategies by abundant numerical tests.

The proposed non-splitting SL HWENO schemes adopt the weak formulation of the SL DG method [18, 5], which comes from the characteristic Galerkin method [10, 32], to update the zeroth-order and first-order moments. In other words, we define the solution space as a  $P^1$  DG space. However, through the HWENO reconstructions, the  $P^1$  DG solution is replaced with a piecewise  $P^3$  polynomial for the solution evaluation. Such a procedure can be viewed as a  $P_N P_M$  method introduced in [12]. The combination of the weak formulation of SL DG method and the HWENO reconstruction can also be regarded as a one-step evolution Galerkin scheme introduced in [24]. The proposed SL scheme requires a remapping procedure between a fixed Eulerian mesh and a characteristic upstream twisted mesh. To accomplish a fourth-order accuracy, the remapping procedure can be summarized in the following three steps. Firstly, we define a cubic-curved numerical upstream mesh to approximate the real upstream mesh. Secondly, a clipping technique is involved to gather the curved polygons generated from the Eulerian mesh and the cubic-curved mesh. Finally, apply piecewise integration over each cubic-curved upstream cell. For nonlinear models, we couple the proposed SL HWENO schemes with a fourth-order Runge-Kutta exponential integrator (RKEI) [8], which freezes the velocity field for each stage, for high-order temporal accuracy. Notice that the evaluation of zeroth-order moment (cell average) is equivalent to the formulation of the SL finite volume (FV) method in [42]. The mass conservation, positivity preservation (PP), and fourth-order accuracy can be proved similar to [42]. For stability, under a linearized setting, we numerically prove the unconditionally stable property of the proposed schemes by the Fourier analysis.

An outline of this paper is as follows. In Section 2, we introduce the construction of the SL

HWENO schemes. In Section 3, we describe how to couple the proposed SL HWENO scheme with the fourth-order RKEI method for nonlinear models. A variety of numerical tests are provided in Section 4. Finally, a conclusion is presented in Section 5.

## 2. Two-dimensional SL HWENO schemes

Consider the following linear transport equation

$$u_t + (a(x, y, t)u)_x + (b(x, y, t)u)_y = 0, \quad (2.1)$$

where  $(a(x, y, t), b(x, y, t))$  represents a known velocity field and  $u(x, y, t)$  is a density function. We assume a rectangle computational domain  $\Omega := [x_L, x_R] \times [y_B, y_T]$  and a corresponding discretization such that  $x_L = x_{\frac{1}{2}} < x_{\frac{3}{2}} < \dots < x_{N_x + \frac{1}{2}} = x_R$ ,  $y_B = y_{\frac{1}{2}} < y_{\frac{3}{2}} < \dots < y_{N_y + \frac{1}{2}} = y_T$ , with  $I_i^x := [x_{i-\frac{1}{2}}, x_{i+\frac{1}{2}}]$ ,  $I_j^y := [y_{j-\frac{1}{2}}, y_{j+\frac{1}{2}}]$ ,  $I_{i,j} := I_i^x \times I_j^y$ ,  $x_i := \frac{x_{i-\frac{1}{2}} + x_{i+\frac{1}{2}}}{2}$ ,  $y_j := \frac{y_{j-\frac{1}{2}} + y_{j+\frac{1}{2}}}{2}$ ,  $\Delta x_i := x_{i+\frac{1}{2}} - x_{i-\frac{1}{2}}$  and  $\Delta y_j := y_{j+\frac{1}{2}} - y_{j-\frac{1}{2}}$ . We define a  $P^1$  DG solution space  $V_h^1 := \{u_h | u_h(x, y)|_{I_{i,j}} \in P^1(I_{i,j}) \forall i, j\}$ . Consider an Eulerian cell  $I_{i,j}$  at  $t = t^{n+1}$  and define a dynamic characteristic region  $I_{i,j}(t) := \{(x^*, y^*) | (x^*, y^*) = (X(x, y; t), Y(x, y; t)), (x, y) \in I_{i,j}\}$ , where  $(X(x, y; t), Y(x, y; t))$  represents the characteristic curve emanating from  $(x, y, t^{n+1})$ , i.e., the solution of the ordinary differential equations (ODEs)

$$\begin{cases} dX(t)/dt = a(X(t), Y(t), t), \\ dY(t)/dt = b(X(t), Y(t), t), \\ X(t^{n+1}) = x, \\ Y(t^{n+1}) = y. \end{cases} \quad (2.2)$$

We define an adjoint problem of (2.1) as in [10, 32] on  $I_{i,j}(t) \times [t^n, t^{n+1}]$ : for a given test function  $W(x, y) \in P^1(I_{i,j})$ ,

$$\begin{cases} w_t + a(x, y, t)w_x + b(x, y, t)w_y = 0, & t \in [t^n, t^{n+1}) \\ w(t = t^{n+1}) = W(x, y). \end{cases} \quad (2.3)$$

By the Reynolds transport Theorem, we have,

$$\frac{d}{dt} \iint_{I_{i,j}(t)} u(x, y, t)w(x, y, t) dx dy = 0. \quad (2.4)$$

From (2.4), an SL scheme is naturally formulated:

$$\frac{1}{\Delta x_i \Delta y_j} \iint_{I_{i,j}} u(x, y, t^{n+1})W(x, y) dx dy = \frac{1}{\Delta x_i \Delta y_j} \iint_{I_{i,j}^*} u(x, y, t^n)w(x, y, t^n) dx dy, \quad (2.5)$$

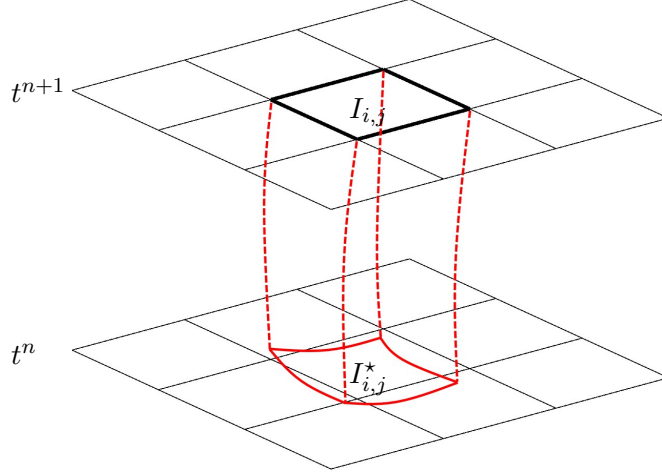


Figure 2.1: Schematic illustration for the characteristic upstream cell  $I_{i,j}^*$ .

where  $I_{i,j}^* = I_{i,j}(t^n)$  (see Figure 2.1). For given time level  $t^n$ , we denote the first three moments of the solution by  $\{\bar{u}_{i,j}\}$ ,  $\{\bar{v}_{i,j}\}$ , and  $\{\bar{w}_{i,j}\}$ . Then, we denote the numerical solution on  $t^n$  by  $u^n$  with

$$u^n(x, y) = \bar{u}_{i,j} + 12\bar{v}_{i,j} \left( \frac{x - x_i}{\Delta x_i} \right) + 12\bar{w}_{i,j} \left( \frac{y - y_j}{\Delta y_j} \right), \quad (x, y) \in I_{i,j}. \quad (2.6)$$

For constructing an SL HWENO scheme, it is sufficient to take  $W(x, y) = 1$ ,  $(x - x_i)/\Delta x_i$ ,  $(y - y_j)/\Delta y_j$  and evaluate the right-hand side of (2.5) accurately. To approximate the right-hand side of (2.5), in Section 2.1, we first introduce the two newly constructed HWENO reconstructions to recover a piece-wise cubic polynomial, denoted by  $H^n(x, y)$ , to approximate  $u(x, y, t^n)$  in (2.5). Then, in Section 2.2, cubic-curved quadrilaterals, denoted by  $\{\tilde{I}_{i,j}^*\}$ , are defined for approximating  $\{I_{i,j}^*\}$  and a cubic polynomial  $\tilde{w}(x, y)$  is constructed over each  $\tilde{I}_{i,j}^*$  by a least square procedure to approximate the test function  $w(x, y)$ . Finally, we briefly summarize the integration strategy on  $\tilde{I}_{i,j}^*$  in Section 2.3.

### 2.1. Two-dimensional HWENO reconstruction methods

For convenience, we require  $\Delta x_i \equiv \Delta x$ ,  $\Delta y_j \equiv \Delta y \quad \forall i, j$ . Based on the  $P^1$  DG solution,  $u^n(x, y)$ , we recover a piecewise  $P^3$  polynomial,

$$H^n(x, y) = H^{(i,j)}(x, y), \quad (x, y) \in I_{i,j}, \quad \forall (i, j), \quad (2.7)$$

where  $H^{(i,j)}(x, y) \in P^3(I_{i,j})$ . We define a set of local orthogonal basis of the high order polynomial denoted as  $\{P_l(x, y)\}$  with:

$$\begin{aligned}
P_1(x, y) &= 1, & P_2(x, y) &= \mu_i(x) := \frac{x - x_i}{\Delta x}, & P_3(x, y) &= \nu_j(y) := \frac{y - y_j}{\Delta y}, \\
P_4(x, y) &= \mu_i^2 - \frac{1}{12}, & P_5(x, y) &= \mu_i \nu_j, & P_6(x, y) &= \nu_j^2 - \frac{1}{12}, \\
P_7(x, y) &= \mu_i^3 - \frac{3}{20} \mu_i, & P_8(x, y) &= \left( \mu_i^2 - \frac{1}{12} \right) \nu_j, & P_9(x, y) &= \mu_i \left( \nu_j^2 - \frac{1}{12} \right), \\
P_{10}(x, y) &= \nu_j^3 - \frac{3}{20} \nu_j, & P_{11}(x, y) &= \left( \mu_i^2 - \frac{1}{12} \right) \left( \nu_j^2 - \frac{1}{12} \right).
\end{aligned} \tag{2.8}$$

We also define that  $\bar{u}_5^n := \bar{u}_{i,j}^n$ ,  $\bar{v}_5^n := \bar{v}_{i,j}^n$ ,  $\bar{w}_5^n := \bar{w}_{i,j}^n$ ,  $I_5 := I_{i,j}$  and other  $\{\bar{u}_s^n\}$ ,  $\{\bar{v}_s^n\}$ ,  $\{\bar{w}_s^n\}$ ,  $\{I_s\}$  represent corresponding moments and Eulerian cells based on the serial numbers in Figure 2.2. Then, the 2-D HWENO reconstruction methods over  $I_{i,j}$  are summarized as follows.

$j + 1$	7	8	9
$j$	4	5	6
$j - 1$	1	2	3
	$i - 1$	$i$	$i + 1$

Figure 2.2: Stencil for the HWENO reconstructions on 2-D Cartesian mesh.

**Step 1.** Reconstruct the first-order moments.

The first-order moments,  $\{\bar{v}_5^n, \bar{w}_5^n\}$ , can be extremely large when  $u(x, y, t^n)$  is discontinuous in  $I_{i,j}$  since  $\bar{v}_5^n \sim \frac{\Delta x}{12} \frac{\partial u}{\partial x}|_{(x_i, y_j)}$  and  $\bar{w}_5^n \sim \frac{\Delta y}{12} \frac{\partial u}{\partial y}|_{(x_i, y_j)}$ . Hence, before recovering a cubic polynomial, we reconstruct the first-order moments with the following two goals: it will provide high-order approximations of first-order moments when  $u(x, y, t^n)$  is smooth in  $I_{i,j}$ ; when  $u(x, y, t^n)$  is discontinuous in  $I_{i,j}$ , first-order moments will be reduced to a reasonable level.

The two first-order moments can be regarded as local indicators of the changing rates for the  $x$ - and  $y$ -dimensions. Each of them is highly independent of the other dimension. Hence, the reconstruction is performed in a dimension-by-dimension manner. Below, we take the  $x$  direction as an example to illustrate the procedure for reconstructing its first-order moment.

**Step 1.1.** Compute approximations to the first-order moment and smoothness indicators from 1-D polynomial reconstructions.

1. Construct a quartic polynomial  $p_0(x)$ , and three quadratic polynomials  $\{p_k(x)\}_{k=1}^3$  satisfying

$$\begin{aligned} \frac{1}{\Delta x} \int_{I_{i+l}^x} p_0(x) dx &= \bar{u}_{i+l,j}^n, \quad l = -1, 0, 1, \\ \frac{1}{\Delta x} \int_{I_{i+l}^x} p_0(x) \left( \frac{x - x_{i+l}}{\Delta x} \right) dx &= \bar{v}_{i+l,j}^n, \quad l = -1, 1, \end{aligned} \quad (2.9)$$

and

$$\begin{aligned} \frac{1}{\Delta x} \int_{I_{i+l}^x} p_1(x) dx &= \bar{u}_{i+l,j}^n \quad l = -1, 0, \quad \frac{1}{\Delta x} \int_{I_{i-1}^x} p_1(x) \left( \frac{x - x_{i-1}}{\Delta x} \right) dx = \bar{v}_{i-1,j}^n; \\ \frac{1}{\Delta x} \int_{I_{i+l}^x} p_2(x) dx &= \bar{u}_{i+l,j}^n \quad l = -1, 0, 1; \\ \frac{1}{\Delta x} \int_{I_{i+l}^x} p_3(x) dx &= \bar{u}_{i+l,j}^n \quad l = 0, 1, \quad \frac{1}{\Delta x} \int_{I_{i+1}^x} p_1(x) \left( \frac{x - x_{i+1}}{\Delta x} \right) dx = \bar{v}_{i+1,j}^n. \end{aligned} \quad (2.10)$$

2. Compute the first-order moments of  $\{p_k(x)\}_{k=0}^3$ :

$$\begin{aligned} \tilde{v}_{i,j,0}^n &:= \frac{1}{\Delta x} \int_{I_i^x} p_0(x) \left( \frac{x - x_i}{\Delta x} \right) dx = -\frac{5}{76} \bar{u}_{i-1,j}^n - \frac{11}{38} \bar{v}_{i-1,j}^n - \frac{11}{38} \bar{v}_{i+1,j}^n + \frac{5}{76} \bar{u}_{i+1,j}^n, \\ \tilde{v}_{i,j,1}^n &:= \frac{1}{\Delta x} \int_{I_i^x} p_1(x) \left( \frac{x - x_i}{\Delta x} \right) dx = \frac{1}{6} \bar{u}_{i,j}^n - \frac{1}{6} \bar{u}_{i-1,j}^n - \bar{v}_{i-1,j}^n, \\ \tilde{v}_{i,j,2}^n &:= \frac{1}{\Delta x} \int_{I_i^x} p_2(x) \left( \frac{x - x_i}{\Delta x} \right) dx = \frac{1}{24} \bar{u}_{i+1,j}^n - \frac{1}{24} \bar{u}_{i-1,j}^n, \\ \tilde{v}_{i,j,3}^n &:= \frac{1}{\Delta x} \int_{I_i^x} p_2(x) \left( \frac{x - x_i}{\Delta x} \right) dx = \frac{1}{6} \bar{u}_{i+1,j}^n - \frac{1}{6} \bar{u}_{i,j}^n - \bar{v}_{i+1,j}^n. \end{aligned} \quad (2.11)$$

3. Compute the smoothness indicators  $\{\beta_k\}_{k=0}^3$  of  $\{p_k(x)\}_{k=0}^3$  [23, 21, 33]:

$$\beta_k = \sum_{l=1}^r \frac{1}{\Delta x} \int_{I_i^x} \left( \Delta x^l \frac{\partial^l}{\partial x^l} p_k(x) \right)^2 dx \quad k = 0, 1, 2, 3 \quad (2.12)$$

with  $r$  representing the degree of the corresponding polynomial. Here, the smoothness indicators  $\{\beta_k\}_{k=1}^3$  can be explicitly expressed by

$$\begin{aligned} \beta_1 &= \left( 12 \tilde{v}_{i,j,1}^n \right)^2 + 156 \left( \tilde{v}_{i,j,1}^n - \bar{v}_{i-1,j}^n \right)^2, \\ \beta_2 &= \left( 12 \tilde{v}_{i,j,2}^n \right)^2 + \frac{13}{12} \left( \bar{u}_{i+1,j}^n - 2 \bar{u}_{i,j}^n + \bar{u}_{i-1,j}^n \right)^2, \\ \beta_3 &= \left( 12 \tilde{v}_{i,j,3}^n \right)^2 + 156 \left( \bar{v}_{i+1,j}^n - \tilde{v}_{i,j,3}^n \right)^2. \end{aligned} \quad (2.13)$$

We refer to [40] for the explicit expression of  $\beta_0$ .



4. Compute a full stencil global reference smoothness indicator [20]:

$$\tau := \left( \frac{|\beta_0 - \beta_1| + |\beta_0 - \beta_3|}{2} \right)^2. \quad (2.14)$$

By the Taylor expansion, we can find that  $\tau = O(\Delta x^6)$ , if there is no discontinuity involved.

**Step 1.2** Weight the collected first-order moments.

Below, we first introduce the weighting strategy for the HWENO-1.

1. Compute the nonlinear weights by

$$\omega_k = \frac{\bar{\omega}_k}{\sum_l \bar{\omega}_l} \quad \text{with} \quad \bar{\omega}_k = \gamma_k \left( 1 + \frac{\tau}{\beta_k + \epsilon} \right) \quad k = 0, 1, 3, \quad (2.15)$$

where  $\epsilon = 10^{-40}$  is set to avoid the denominator being zero. The linear weights,  $\{\gamma_0, \gamma_1, \gamma_3\}$ , are chosen as  $\{0.6, 0.2, 0.2\}$  in this paper. We refer to [43, 40] for more details on linear and nonlinear weights.

2. Reconstruct the  $x$ -dimension first-order moment,  $\bar{v}_5^n$ , by:

$$\bar{v}_5^n = \frac{\omega_0}{\gamma_0} \left( \tilde{v}_{i,j,0}^n - \gamma_1 \tilde{v}_{i,j,1}^n - \gamma_3 \tilde{v}_{i,j,3}^n \right) + \omega_1 \tilde{v}_{i,j,1}^n + \omega_3 \tilde{v}_{i,j,3}^n. \quad (2.16)$$

The HWENO-2 reconstructs the first-order moment  $\bar{v}_5^n$  as follows.

1. Separate the discontinuities from broad-band smooth fluctuations as illustrated in [16, 15] by first taking

$$\eta_k = \left( 1 + \frac{\tau}{\beta_k + \epsilon} \right)^6 \quad k = 1, 2, 3, \quad (2.17)$$

where  $\epsilon = 10^{-40}$  is used to avoid the denominator being zero as in [2]. If there is no discontinuity involved, we can find that  $\eta_k \approx 1$  for all  $k$ . If there is discontinuity involved for the global three-cells stencil, the  $\eta$  value for a smooth small stencil can be greatly enlarge with a magnitude of  $O(\Delta x^{-12})$ . Then, we normalize  $\{\eta_k\}_{k=1}^3$  with

$$\kappa_k = \frac{\eta_k}{\sum_{l=1}^3 \eta_l} \quad k = 1, 2, 3. \quad (2.18)$$

2. Reconstruct the  $x$ -dimension first-order moment  $\bar{v}_5^n$  by:

$$\bar{v}_5^n = \tilde{v}_{i,j,0}^n, \quad \text{if} \quad \min_k \kappa_k > C_T, \quad (2.19)$$

otherwise

$$\tilde{v}_5^n = \begin{cases} \tilde{v}_{i,j,1}^n, & \text{if } \kappa_1 > \kappa_3, \\ \tilde{v}_{i,j,3}^n, & \text{if } \kappa_3 > \kappa_1. \end{cases} \quad (2.20)$$

where  $C_T$  is a parameter deciding whether a corresponding polynomial should be involved [16]. We empirically choose  $C_T = 10^{-3}$  as in [20]. For treating discontinuity, unlike [16, 20], we only choose the smoothest polynomial for reconstruction, since the weighted summation does not increase the order of accuracy for our case. When  $\{\kappa_k\}$  matches the smoothness of the three-cells stencil, we directly use  $\tilde{v}_{i,j,0}^n$  for optimal accuracy.

The first-order moment in  $y$  direction can be reconstructed in a similar way; we the reconstructed first-order moment in this direction by  $\tilde{w}_5^n$ .

**Step 2.** Recover the reconstructed  $H^n(x, y)$  on  $I_{i,j}$ .

**Step 2.1.** Collect information from different 2-D polynomials.

1. Construct a polynomial  $\tilde{q}_0(x, y) := \sum_{l=1}^{11} a_l^{q_0} P_l(x, y)$  such that

$$\begin{aligned} \frac{1}{\Delta x \Delta y} \iint_{I_s} \tilde{q}_0(x, y) dx dy &= \bar{u}_s^n, \quad s = 1, 2, \dots, 9, \\ \frac{1}{\Delta x \Delta y} \iint_{I_5} \tilde{q}_0(x, y) \left( \frac{x - x_i}{\Delta x} \right) dx dy &= \tilde{v}_5^n, \\ \frac{1}{\Delta x \Delta y} \iint_{I_5} \tilde{q}_0(x, y) \left( \frac{y - y_j}{\Delta y} \right) dx dy &= \tilde{w}_5^n. \end{aligned} \quad (2.21)$$

Let  $q_0(x, y) = \sum_{l=1}^{10} a_l^{q_0} P_l(x, y)$ , which is the orthogonal projection of  $\tilde{q}_0(x, y)$  to  $P^3(I_{i,j})$ . We provide the explicit expressions of  $\{a_l^{q_0}\}_{l=1}^{10}$  in Appendix A.

2. Construct four quadratic polynomial  $\{q_k(x, y)\}_{k=1}^4 := \{\sum_{l=1}^6 a_l^{q_k} P_l(x, y)\}_{k=1}^4$  satisfying

$$\begin{aligned} \frac{1}{\Delta x \Delta y} \iint_{I_s} q_k(x, y) dx dy &= \bar{u}_s^n, \\ \frac{1}{\Delta x \Delta y} \iint_{I_5} q_k(x, y) \frac{x - x_i}{\Delta x} dx dy &= \tilde{v}_5^n, \\ \frac{1}{\Delta x \Delta y} \iint_{I_5} q_k(x, y) \frac{y - y_j}{\Delta y} dx dy &= \tilde{w}_5^n, \end{aligned} \quad (2.22)$$

where

$$\begin{aligned} s = 1, 2, 4, 5, \quad \text{for } k = 1; \quad s = 2, 3, 5, 6, \quad \text{for } k = 2; \\ s = 4, 5, 7, 8, \quad \text{for } k = 3; \quad s = 5, 6, 8, 9, \quad \text{for } k = 4. \end{aligned} \quad (2.23)$$

The explicit expressions of  $\{a_l^{q_k}\}$  are given in Appendix A.

3. Compute the smoothness indicator [23, 21, 33]  $\{\hat{\beta}_k\}_{k=0}^4$  of  $\{q_k(x, y)\}_{k=0}^4$ :

$$\begin{aligned}\hat{\beta}_0 &= \frac{1}{\Delta x \Delta y} \sum_{l_1+l_2 \leq 3} \iint_{I_{i,j}} \left( \Delta x^{l_1} \Delta y^{l_2} \frac{\partial^{|l_1+l_2|}}{\partial x^{l_1} \partial y^{l_2}} q_0(x, y) \right)^2 dx dy; \\ \hat{\beta}_k &= \frac{1}{\Delta x \Delta y} \sum_{l_1+l_2 \leq 2} \iint_{I_{i,j}} \left( \Delta x^{l_1} \Delta y^{l_2} \frac{\partial^{|l_1+l_2|}}{\partial x^{l_1} \partial y^{l_2}} q_k(x, y) \right)^2 dx dy, \quad k = 1, 2, 3, 4.\end{aligned}\tag{2.24}$$

The explicit expression of  $\{\hat{\beta}_k\}_{k=0}^4$  can be given by

$$\begin{aligned}\hat{\beta}_0 &= \left( a_2^{q_0} + \frac{1}{10} a_7^{q_0} \right)^2 + \left( a_3^{q_0} + \frac{1}{10} a_{10}^{q_0} \right)^2 + \frac{13}{3} (a_4^{q_0})^2 + \frac{7}{6} (a_5^{q_0})^2 + \frac{13}{3} (a_6^{q_0})^2 \\ &\quad + \frac{781}{20} (a_7^{q_0})^2 + \frac{47}{10} (a_8^{q_0})^2 + \frac{47}{10} (a_9^{q_0})^2 + \frac{781}{20} (a_{10}^{q_0})^2; \\ \hat{\beta}_k &= (a_2^{q_k})^2 + (a_3^{q_k})^2 + \frac{13}{3} (a_4^{q_k})^2 + \frac{7}{6} (a_5^{q_k})^2 + \frac{13}{3} (a_6^{q_k})^2 \quad \text{for } k = 1, 2, 3, 4.\end{aligned}\tag{2.25}$$

4. Compute a full stencil global reference smoothness indicator:

$$\hat{\tau} = \left( \frac{|\hat{\beta}_0 - \hat{\beta}_1| + |\hat{\beta}_0 - \hat{\beta}_2| + |\hat{\beta}_0 - \hat{\beta}_3| + |\hat{\beta}_0 - \hat{\beta}_4|}{4} \right)^2.\tag{2.26}$$

Similarly, by the Taylor expansion, we can easily check that  $\hat{\tau} = O(\Delta x^6)$ , if there is no discontinuity involved.

**Step 2.2** Weight the collected 2-D polynomials.

The HWENO-1 weights the polynomials as follows.

1. Compute the nonlinear weights by

$$\hat{\omega}_k = \frac{\tilde{\omega}_k}{\sum_l \tilde{\omega}_l} \quad \text{with} \quad \tilde{\omega}_k = \gamma_k \left( 1 + \frac{\tau}{\beta_k + \epsilon} \right) \quad k = 0, 1, 2, 3, 4,\tag{2.27}$$

where  $\epsilon = 10^{-40}$  is set to avoid the denominator being zero. The linear weights,  $\{\gamma_k\}_{k=0}^4$  are chosen as  $\{0.6, 0.1, 0.1, 0.1, 0.1\}$  in this paper.

2. Construct  $H^{(i,j)}(x, y) := \sum_{l=1}^{10} a_l P_l(x, y)$ :

$$H^{(i,j)}(x, y) = \frac{\hat{\omega}_0}{\hat{\gamma}_0} \left( q_0(x) - \sum_{k=1}^4 \hat{\gamma}_k q_k(x, y) \right) + \sum_{k=1}^4 \hat{\omega}_k q_k(x, y), \quad (x, y) \in I_{i,j}.\tag{2.28}$$

Here, the coefficients  $\{a_l\}$  can be explicitly given by

$$\begin{aligned}a_1 &= \bar{u}_5^n; \quad a_2 = 12\bar{v}_5^n; \quad a_3 = 12\bar{w}_5^n; \\ a_l &= \frac{\hat{\omega}_0}{\hat{\gamma}_0} a_l^{q_0} + \sum_{k=1}^4 \left( \hat{\omega}_k - \frac{\hat{\omega}_0}{\hat{\gamma}_0} \hat{\gamma}_k \right) a_l^{q_k} \quad \text{for } l = 4, 5, 6; \\ a_l &= \frac{\hat{\omega}_0}{\hat{\gamma}_0} a_l^{q_0} \quad \text{for } l = 7, 8, \dots, 10.\end{aligned}\tag{2.29}$$

The HWENO-2 weights the polynomials as follows.

1. Compute the separation parameters  $\{\hat{\eta}_k\}_{k=1}^4$  and the corresponding normalized parameters  $\{\hat{\kappa}_k\}_{k=1}^4$  similarly:

$$\hat{\kappa}_k = \frac{\hat{\eta}_k}{\sum_{l=1}^3 \hat{\eta}_l} \quad \text{with } \hat{\eta}_k = \left(1 + \frac{\hat{\tau}_6}{\hat{\beta}_k + \epsilon}\right)^6 \quad \text{for } k = 1, 2, 3, 4, \quad (2.30)$$

where  $\epsilon = 10^{-40}$ .

2. Construct  $H^{(i,j)}(x, y)$  by

$$H^{(i,j)}(x, y) = q_0(x, y), \quad \text{if } \min_k \hat{\kappa}_k > C_T, \quad (2.31)$$

otherwise

$$H^{(i,j)}(x, y) = q_K(x, y) \quad \text{with } K \text{ being the index such that } \hat{\kappa}_K = \max_k \hat{\kappa}_k. \quad (2.32)$$

Here,  $C_T$  is chosen as  $10^{-3}$ .

In particular, if  $\tilde{v}_{i,j}^n = \tilde{v}_{i,j,0}^n$ ,  $\tilde{w}_{i,j}^n = \tilde{w}_{i,j,0}^n$  (with similar notation), and  $H^{(i,j)}(x, y) = q_0(x, y) \quad \forall i, j$ , we call such a reconstruction linear reconstruction.

## 2.2. Constructing cubic-curved upstream cells and approximating $w(x, y, t^n)$

To evaluate the right-hand side of (2.5), it remains to provide the approximations of  $\{I_{i,j}^*\}$  and  $w(x, y, t^n)$ . For a given index  $(i, j)$ , the cubic-curved quadrilateral upstream cell,  $\tilde{I}_{i,j}^*$ , and the cubic polynomial  $\tilde{w}(x, y)$  on  $\tilde{I}_{i,j}^*$  are constructed by the following procedure.

1. Tracing characteristics backward in time.

We locate  $4 \times 4$  Gauss-Legendre-Lobatto (GLL) points on  $I_{i,j}$ . We determine the characteristic feet of these GLL points by solving (2.2) at  $t = t^n$  (see Figure 2.3). In practice, we solve the ODEs (2.2) by a fourth-order Runge-Kutta (RK) method.

2. Constructing the edges of the cubic-curved quadrilateral upstream cells.

The edges of the cubic-curved quadrilateral upstream cells are constructed by a cubic interpolation procedure (see [42]). In particular, we prefer to use a parametric form to present any cubic-curved edge:

$$\begin{cases} x(\xi) = x_a \xi^3 + x_b \xi^2 + x_c \xi + x_d, \\ y(\xi) = y_a \xi^3 + y_b \xi^2 + y_c \xi + y_d, \quad \xi \in [-1, 1]. \end{cases} \quad (2.33)$$

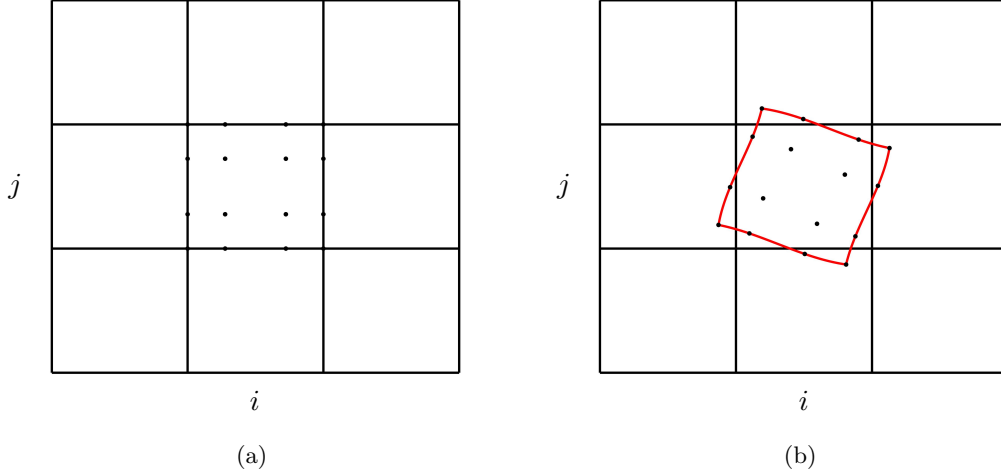


Figure 2.3: Left: the black solid lines represent the Eulerian mesh; the black dots are the GLL points located on the Eulerian cell  $I_{i,j}$ . Right: the black solid lines represent the Eulerian mesh; the red solid lines represent the boundary of  $I_{i,j}^*$ ; the black dots are the characteristic feet obtained by solving (2.2).

### 3. Constructing $\tilde{w}(x, y)$ .

We denote the sixteen GLL points in Figure 2.3 (a) by  $\{v_k\}$  and denote the corresponding characteristic feet by  $\{v_k^*\}$ . By the adjoint problem (2.3), we have

$$w(x(v_k^*), y(v_k^*)) = W(x(v_k), y(v_k)) \quad \text{for } k = 1, 2, \dots, 16. \quad (2.34)$$

Hence, by a standard least square procedure, we can find a cubic polynomial  $\tilde{w}(x, y) \in P^3$ .

#### 2.3. Numerical integration

For numerically evaluating the right-hand side of (2.5), we integrate the piecewise polynomial  $H^n(x, y)\tilde{w}(x, y)$  over each  $\tilde{I}_{i,j}^*$ , which may cross different Eulerian background cells. Hence,  $\tilde{I}_{i,j}^*$  is first clipped into curved polygons such that  $\tilde{I}_{i,j}^* = \cup_{(p,q)}(\tilde{I}_{i,j}^* \cap I_{p,q})$  and the integrand is smooth in each polygon. For conciseness, the curved polygons  $\{\tilde{I}_{i,j}^* \cap I_{p,q}\}$  are denoted by  $\{\tilde{I}_{i,j;p,q}^*\}$ . In particular, we are concerned about the information along the edges of  $\{\tilde{I}_{i,j;p,q}^*\}$ . The edges of  $\{\tilde{I}_{i,j;p,q}^*\}$ , overlapping  $\partial\tilde{I}_{i,j}^*$ , with counterclockwise direction with respect to  $\tilde{I}_{i,j}^*$  are denoted by  $\{\mathcal{L}_{i,j;p,q}^k\}$  (see Figure 2.4 (a)). We call  $\{\mathcal{L}_{i,j;p,q}^k\}$  the *outer integral segments* of the upstream cell  $\tilde{I}_{i,j}^*$ . Similarly, the edges of  $\{\tilde{I}_{i,j;p,q}^*\}$ , overlapping mesh lines, with counterclockwise direction with respect to the corresponding curved polygons are denoted by  $\{\mathcal{S}_{i,j;p,q}^k\}$  (see Figure 2.4 (b)). We call  $\{\mathcal{S}_{i,j;p,q}^k\}$  the *inner integral segments* of  $\tilde{I}_{i,j}^*$ . For implementation, we refer to [42] for more details.

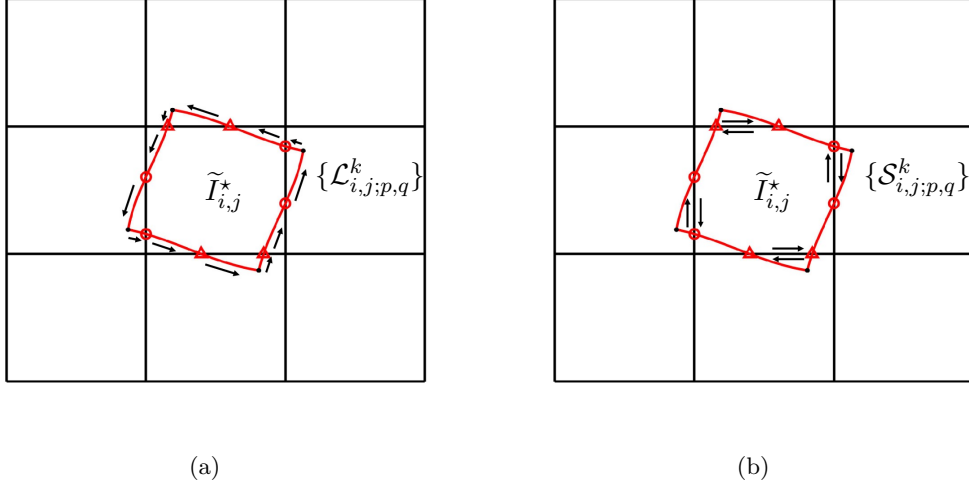


Figure 2.4: Schematic illustration for the outer integral segments (a) and the inner integral segments (b). The red circles and triangles are the intersections of  $\tilde{I}_{i,j}^*$  and the Eulerian mesh.

With the clipped outer integral segments,  $\{\mathcal{L}_{i,j;p,q}^k\}$ , as well as the inner integral segments,  $\{\mathcal{S}_{i,j;p,q}^k\}$ , we evaluate the right-hand side of (2.5) as follows

$$\begin{aligned}
& \frac{1}{\Delta x \Delta y} \iint_{\tilde{I}_{i,j}^*} u(x, y, t^n) w(x, y) dx dy \\
& \approx \frac{1}{\Delta x \Delta y} \iint_{\tilde{I}_{i,j}^*} H^n(x, y) \tilde{w}(x, y) dx dy \\
& = \frac{1}{\Delta x \Delta y} \sum_{(p,q)} \iint_{\tilde{I}_{i,j;p,q}^*} H^{(p,q)}(x, y) \tilde{w}(x, y) dx dy \\
& = \frac{1}{\Delta x \Delta y} \sum_{(p,q)} \int_{\partial(\tilde{I}_{i,j;p,q}^*)} [P dx + Q dy] \\
& = \frac{1}{\Delta x \Delta y} \sum_{(p,q)} \left\{ \sum_k \int_{\mathcal{L}_{i,j;p,q}^k} [P dx + Q dy] + \sum_k \int_{\mathcal{S}_{i,j;p,q}^k} [P dx + Q dy] \right\},
\end{aligned} \tag{2.35}$$

where  $P(x, y)$  and  $Q(x, y)$  are piecewise smooth auxiliary functions such that

$$-\frac{\partial P}{\partial y} + \frac{\partial Q}{\partial x} = H^{(p,q)}(x, y) \tilde{w}(x, y). \tag{2.36}$$

It is straightforward for evaluating the line integral on  $\{\mathcal{S}_{i,j;p,q}^k\}$ . For the integral on an outer integral segment, say  $\mathcal{L}_{i,j;p,q}^k$ ,

$$\int_{\mathcal{L}_{i,j;p,q}^k} [P dx + Q dy] = \int_{\xi_k}^{\xi_{k+1}} [P(x(\xi), y(\xi)) x'(\xi) + Q(x(\xi), y(\xi)) \nu'_q(\xi)] d\xi, \tag{2.37}$$

where  $\xi_k$  and  $\xi_{k+1}$  represent the  $\xi$  value of the start point and end point of  $\mathcal{L}_{i,j;p,q}^k$  (2.33).

The proposed SL HWENO schemes also equip a PP limiter [39], when the analytical solution of (2.1) stays positive. For the implementation of this PP limiter, we refer to [42] for a detailed description.

**Remark 2.1.** We can numerically prove that the numerical update provided by (2.35) is unconditionally stable for linear transport equations with constant coefficients and periodic boundary condition if  $H^n(x, y)$  is reconstructed by the linear reconstruction defined in Section 2.1. The proof is accomplished by the standard von Neumann analysis. We arrange this proof in Appendix B.

### 3. SL HWENO schemes for nonlinear models

The non-splitting SL HWENO schemes are coupled with a fourth-order RKEI in the same framework as in [4] to solve nonlinear models such as the Vlasov-Poisson system, the guiding center Vlasov model, and the incompressible Euler equations in the vorticity-stream function. Below, we briefly describe these three models.

Arising from collisionless plasma, the Vlasov-Poisson system reads

$$f_t + v f_x + E(x, t) f_v = 0, \quad (3.1)$$

$$E(x, t) = -\phi_x, \quad -\phi_{xx}(x, t) = \rho(x, t), \quad (3.2)$$

where  $x$  represents the spatial position,  $v$  is the velocity,  $f(x, v, t)$  is the probability distribution function describing the probability of a particle arises at position  $x$  with velocity  $v$  at time  $t$ . The electric field  $E$  is determined by the Poisson's equation (3.2).  $\phi$  is the self-consistent electrostatic potential.  $\rho = \int_{\mathbb{R}} f(x, v, t) dv - \rho_0$  is the charge density with  $\rho_0 = \frac{1}{|\Omega_x|} \int_{\Omega_x} \int_{\mathbb{R}} f(x, v, 0) dv dx$ .

The 2-D guiding center Vlasov model describes highly magnetized plasma in the transverse plane of a tokamak [38, 14], which can be written as:

$$\rho_t + \nabla \cdot (\mathbf{E}^\perp \rho) = 0, \quad (3.3)$$

$$-\Delta \Phi = \rho, \quad \mathbf{E}^\perp = (-\Phi_y, \Phi_x), \quad (3.4)$$

where  $\rho(x, y, t)$  is the charge density and  $\mathbf{E}$  is the electric field depends on  $\rho$  via the Poisson's equation (3.4).

The 2-D incompressible Euler equation in vorticity-stream function formulation reads

$$\omega_t + \nabla \cdot (\mathbf{u}\omega) = 0, \quad (3.5)$$

$$\Delta\psi = \omega, \quad \mathbf{u} = (-\psi_y, \psi_x), \quad (3.6)$$

where  $\omega(x, y, t)$  is the vorticity of the fluid,  $\mathbf{u} := (u_1, u_2)$  is the velocity field, and  $\psi$  is the stream-function determined by Poisson's equation (3.6).

Notice that these three models can be written in the form of

$$u_t + \nabla \cdot (\mathbf{V}(u(\mathbf{x}, t))u) = 0, \quad (3.7)$$

where  $\mathbf{V}(u(\mathbf{x}, t))$  represents the velocity field. We briefly summarize the SL HWENO scheme coupled with the fourth-order RKEI as follows.

$$\begin{aligned} \bar{u}^{(1)} &= \bar{u}^n \\ \bar{u}^{(2)} &= SLHWENO\left(\frac{1}{2}\mathbf{V}(\bar{u}^{(1)}), \Delta t\right)\bar{u}^n \\ \bar{u}^{(3)} &= SLHWENO\left(\frac{1}{2}\mathbf{V}(\bar{u}^{(2)}), \Delta t\right)\bar{u}^n \\ \bar{u}^{(4)} &= SLHWENO\left(-\frac{1}{2}\mathbf{V}(\bar{u}^{(1)}) + \mathbf{V}(\bar{u}^{(3)}), \Delta t\right)\bar{u}^{(2)} \\ \bar{u}^{n+1} &= SLHWENO\left(-\frac{1}{12}\mathbf{V}(\bar{u}^{(1)}) + \frac{1}{6}\mathbf{V}(\bar{u}^{(2)}) + \frac{1}{6}\mathbf{V}(\bar{u}^{(3)}) + \frac{1}{4}\mathbf{V}(\bar{u}^{(4)}), \Delta t\right) \\ &\quad SLHWENO\left(\frac{1}{4}\mathbf{V}(\bar{u}^{(1)}) + \frac{1}{6}\mathbf{V}(\bar{u}^{(2)}) + \frac{1}{6}\mathbf{V}(\bar{u}^{(3)}) - \frac{1}{12}\mathbf{V}(\bar{u}^{(4)}), \Delta t\right)\bar{u}^n, \end{aligned} \quad (3.8)$$

where  $SLHWENO(\mathbf{V}(\bar{u}^{(k)}), \frac{1}{2}\Delta t)\bar{u}^{(l)}$  represents the solution evolved from  $\bar{u}^{(l)}$  with time step  $\frac{1}{2}\Delta t$  and velocity field  $\mathbf{V}(\bar{u}^{(k)})$  by a non-splitting SL HWENO scheme. For approximating the velocity field, we use Fast Fourier transform to solve the Poisson's equations.

## 4. Numerical tests

### 4.1. Linear transport equations

In this subsection, we test two benchmark problems: transport equation with constant coefficients and the swirling deformation flow. As a comparison, we test the HWENO reconstruction in [40] with their  $p_0(x, y) \in P^4$  replaced by the  $q_0(x, y) \in P^3$  in this paper. Then, the corresponding HWENO reconstruction is denoted by HWENO-old. Through out the tests below, we aim to present the performance of the SL HWENO schemes and compare the differences between different HWENO reconstructions.

Unless specified, we set  $\Delta t = \frac{\text{CFL}}{\frac{\max\{|a(x, y, t)|\}}{\Delta x} + \frac{\max\{|b(x, y, t)|\}}{\Delta y}}$  and  $\text{CFL} = 10.2$ . The PP limiter is applied for the problems with non-negative initial conditions.



**Example 4.1.** (Transport equation with constant coefficients). Consider

$$u_t + u_x + u_y = 0, \quad x \in [-\pi, \pi], \quad y \in [-\pi, \pi], \quad (4.1)$$

with a smooth initial condition,  $u(x, y, 0) = \sin(10(x + y))$ , and the periodic boundary condition. The exact solution for this problem is  $u(x, y, t) = \sin(10(x + y - 2t))$ . In Table 4.1, we present the  $L^2$  errors and corresponding orders of accuracy for the SL HWENO-1, HWENO-2, and HWENO-old schemes. As shown, all the schemes converge to fourth-order accuracy. However, the SL HWENO-old scheme requires a denser mesh to obtain a normal accuracy. In Figure 4.5, we show the cross-section of the numerical solution at  $x = y$  of the three schemes at  $T = 20$  with a fixed mesh of  $80 \times 80$ . With four points per wavelength at  $x = y$ , we observe that HWENO-old tends to be more smeared than the other two.

Table 4.1: (Transport equation with constant coefficients).  $L^2$  errors and corresponding orders of accuracy of the SL HWENO schemes for (4.1) with  $u(x, y, 0) = \sin(10(x + y))$  at  $T = 20$ .

mesh	HWENO-1		HWENO-2		HWENO-old	
	$L^2$ error	order	$L^2$ error	order	$L^2$ error	order
$20 \times 20$	7.07E-01	—	7.07E-01	—	7.07E-01	—
$40 \times 40$	1.59E-01	2.15	2.35E-01	1.59	6.99E-01	0.02
$80 \times 80$	1.71E-02	3.78	1.71E-02	3.78	1.54E-01	2.18
$160 \times 160$	1.13E-03	3.93	1.13E-03	3.93	1.61E-03	6.58
$320 \times 320$	7.07E-05	4.00	7.07E-05	4.00	7.30E-05	4.47

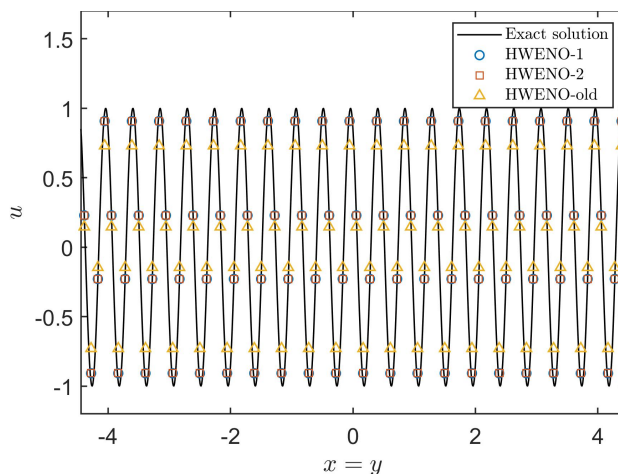


Figure 4.5: (Transport equation with constant coefficients). Cross-sections of SL HWENO solutions at  $T = 20$  at  $x = y$  for (4.1) with  $u(x, y, 0) = \sin(x + y)$  at  $T = 20$  with a mesh of  $80 \times 80$ .

**Example 4.2.** (Swirling deformation flow). Consider

$$u_t - (2\pi\cos^2(\frac{x}{2})\sin(y)g(t)u)_x + (2\pi\sin(x)\cos^2(\frac{y}{2})g(t)u)_y = 0, \quad (4.2)$$

$$x \in [-\pi, \pi], \quad y \in [-\pi, \pi],$$

where  $g(t) = \cos(\pi t/T)$  with  $T = 1.5$ . We consider (4.2) with the following smooth initial condition

$$u(x, y, 0) = \begin{cases} r_0^b \cos(\frac{r^b(\mathbf{x})\pi}{2r_0^b})^6 & \text{if } r^b(\mathbf{x}) < r_0^b, \\ 0, & \text{otherwise,} \end{cases} \quad (4.3)$$

where  $r_0^b = 0.3\pi$ ,  $r^b(\mathbf{x}) = \sqrt{(x - x_0^b)^2 + (y - y_0^b)^2}$  and the center of the cosine bell  $(x_0^b, y_0^b) = (0.3\pi, 0)$ . Zero boundary condition is equipped for this test. In Table 4.2, we present the  $L^2$  errors and corresponding orders of accuracy of the SL HWENO-1, HWENO-2, and HWENO-old schemes. As shown, the SL HWENO schemes are of fourth-order accuracy. The HWENO-1 shows the best convergence rate comparing with the other two HWENO reconstructions. The convergence rate of the HWENO-old is worst. This leads to the same conclusion that HWENO-old reconstruction smears more information. In Figure 4.6, we show the temporal order of accuracy of the SL HWENO-1 scheme by fixing the spatial mesh while varying the time step  $\Delta t$ . We find that the temporal order reaches fifth-order, which is one order higher than the expected fourth-order, for the swirling deformation flow.

Table 4.2: (Swirling deformation flow).  $L^2$  errors and corresponding orders of accuracy of the SL HWENO schemes for (4.2) with initial condition (4.3) at  $t = 1.5$ .

mesh	<b>HWENO-1</b>		<b>HWENO-2</b>		<b>HWENO-old</b>	
	$L^2$ error	order	$L^2$ error	order	$L^2$ error	order
20 × 20	1.57E-02	—	1.59E-02	—	2.76E-02	—
40 × 40	9.57E-04	4.04	1.70E-03	3.22	7.35E-03	1.91
80 × 80	1.32E-04	2.85	2.79E-04	2.61	7.84E-04	3.23
160 × 160	5.25E-06	4.66	2.75E-05	3.34	5.54E-05	3.82
320 × 320	2.23E-07	4.56	1.52E-06	4.18	8.14E-06	2.77
640 × 640	9.03E-09	4.63	6.45E-08	4.56	6.32E-07	3.69
1280 × 1280	4.12E-10	4.45	4.12E-10	7.29	8.07E-09	6.29
2560 × 2560	2.25E-11	4.20	2.25E-11	4.20	2.52E-11	8.32

To investigate the performances of the SL HWENO schemes for discontinuous solutions, we test (4.2) with the initial condition shown in Figure 4.7. We show the mesh plots of the numerical solutions of the SL HWENO schemes at  $t = 0.75$  and at  $t = 1.5$  in Figure 4.8 with a mesh of  $100 \times 100$ . In Figure 4.9, we present two cross-sections of the numerical solutions of the SL HWENO schemes at  $t = 1.5$  with a mesh of  $100 \times 100$ . As shown, the SL HWENO schemes

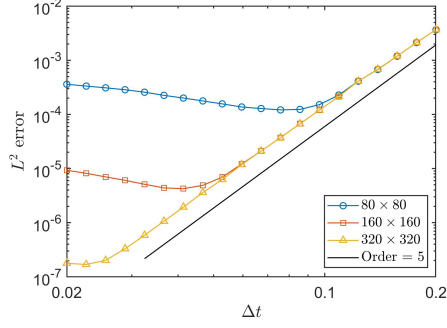


Figure 4.6: (Swirling deformation flow). Temporal order of accuracy of the SL HWENO-1 scheme. The three colored lines use different mesh of  $80 \times 80$ ,  $160 \times 160$ , and  $320 \times 320$ . The programs stop at  $t = 1.5$ .

preserve the geometry of the solution. The SL HWENO-1 scheme and HWENO-2 schemes have better resolution but produces small numerical oscillation at the same time. In Figure 4.9, we observe that the SL HWENO-old scheme is more dissipative than the other two.

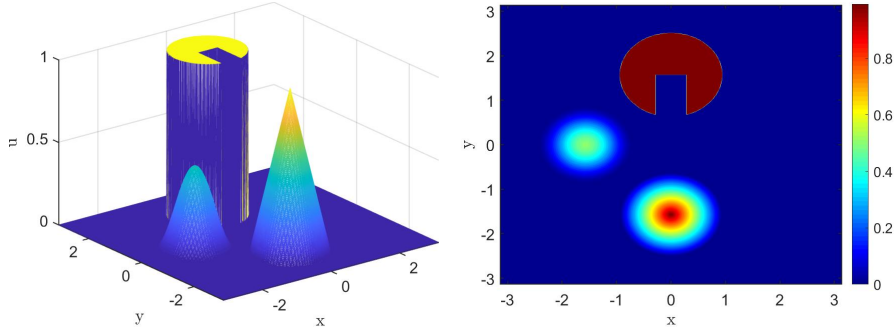


Figure 4.7: (Swirling deformation flow). The mesh plot (left) and the contour plot (right) of the discontinuous initial data for (4.2).

#### 4.2. Nonlinear Vlasov-Poisson system

In this subsection, we test two benchmark tests: the strong Landau damping and the bump-on-tail instability. Unless specified, we set  $N_x = 128$ ,  $N_v = 256$ ,  $CFL = 10.2$ ,  $\Delta t = CFL / (v_{\max}/\Delta x + \max\{|E|\}/\Delta v)$  with  $v_{\max}$  represents the positive boundary of  $v$ -direction. The PP limiter is equipped for both tests.

**Example 4.3.** (Strong Landau damping). Consider the VP system with the initial condition

$$f(x, v, t = 0) = \frac{1}{\sqrt{2\pi}} (1 + \alpha \cos(kx)) \exp\left(-\frac{v^2}{2}\right), \quad x \in [0, 4\pi], \quad v \in [-2\pi, 2\pi], \quad (4.4)$$

where  $k = 0.5$ ,  $\alpha = 0.5$ . In Table 4.3, we show the  $L^2$  errors and corresponding orders of accuracy of the SL HWENO schemes for the strong Landau damping at  $T = 2$ . The errors are obtained

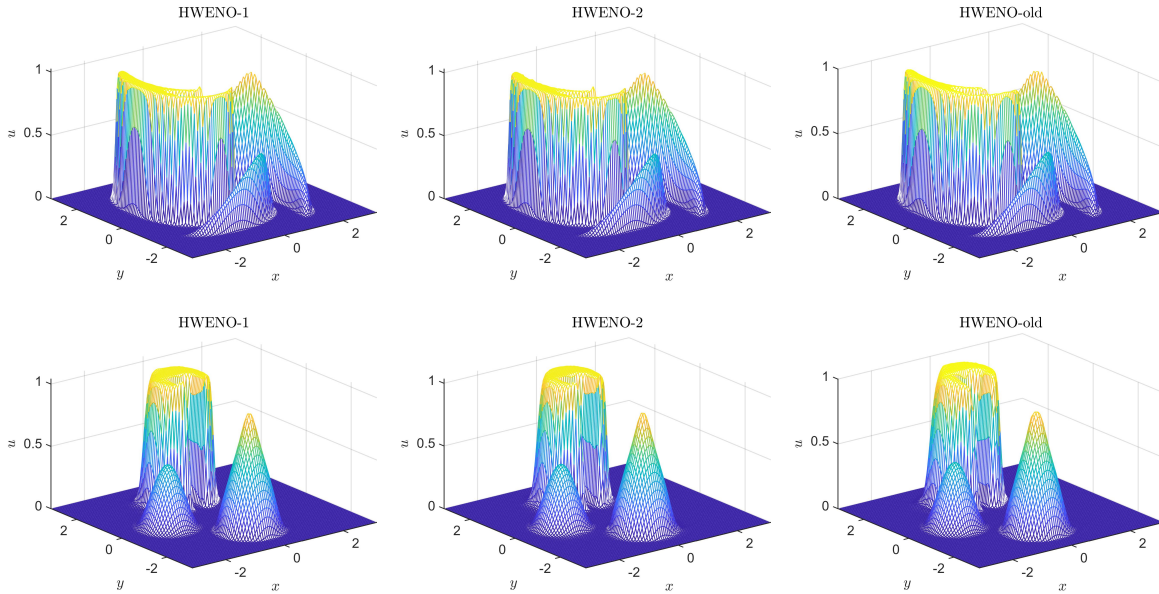


Figure 4.8: (Swirling deformation flow). The mesh plots of the numerical solutions of the SL HWENO-1 (left), HWENO-2 (middle), and HWENO-old (right) schemes for (4.2) with initial condition Figure 4.7 at  $t = 0.75$  (top) and at  $t = 1.5$  (bottom) with a mesh of  $100 \times 100$ .

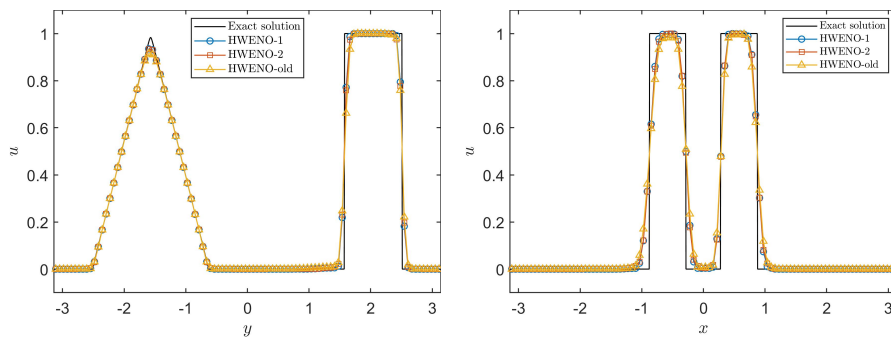


Figure 4.9: (Swirling deformation flow). Cross-sections of the SL HWENO solutions at  $x = 0$  (left) and  $y = 1.2$  (right) at  $t = 1.5$  with a mesh of  $100 \times 100$ .

by comparing the solution to a reference solution with mesh refinement. We observe the expected order of accuracy and the three reconstructions perform similarly for this test. In Figure 4.10, we present the temporal order of accuracy of the SL HWENO-1 scheme by fixing the spatial mesh while varying  $\Delta t$ . We observe a clear fourth-order temporal accuracy.

Table 4.3: (Strong Landau damping).  $L^2$  errors and corresponding orders of accuracy of the SL HWENO schemes at  $T = 2$ .

mesh	HWENO-1		HWENO-2		HWENO-old	
	$L^2$ error	order	$L^2$ error	order		
$16 \times 16$	4.29E-03	—	4.22E-03	—	5.07E-03	—
$32 \times 32$	4.52E-04	3.25	4.47E-04	3.24	4.70E-04	3.43
$64 \times 64$	2.10E-05	4.43	2.10E-05	4.42	1.91E-05	4.62
$128 \times 128$	6.15E-07	5.10	6.15E-07	5.09	6.12E-07	4.97
$256 \times 256$	2.69E-08	4.51	2.70E-08	4.51	2.69E-08	4.51

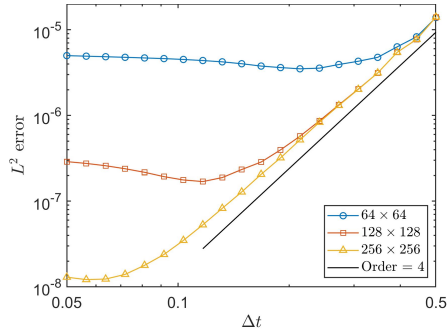


Figure 4.10: (Strong Landau damping). Temporal order of accuracy of the SL HWENO-1 scheme. The three colored lines use different mesh of  $64 \times 64$ ,  $128 \times 128$ , and  $256 \times 256$ . The programs stop at  $T = 2$ .

In Figure 4.11, we present the mesh plots and contour plots of numerical solutions of the SL HWENO schemes at  $T = 40$ . We observe that the numerical solution maintains the filamentation structure well for the strong Landau damping. In Figure 4.12, the cross-sections of the SL HWENO schemes at  $T = 40$  and at  $x = 2\pi$  are provided. We observe slightly better resolution for the SL HWENO-1 and HWENO-2 schemes.

The VP system has several conservative quantities such as mass,  $L^p$  norms, energy, and entropy [31]. We can observe a  $O(10^{-12})$  level of relative deviation of mass and  $L^1$  norm with  $v_{\max} = 10$  for strong Landau damping as shown in Figure 4.13. For  $L^2$  norm, energy, and entropy, we present the relative deviations of them for the SL HWENO schemes in Figure 4.14. As shown, the magnitude of deviations are similar to the existing results [31, 29].

**Example 4.4.** (Bump-on-tail instability [1, 5]). Consider the bump-on-tail instability with the

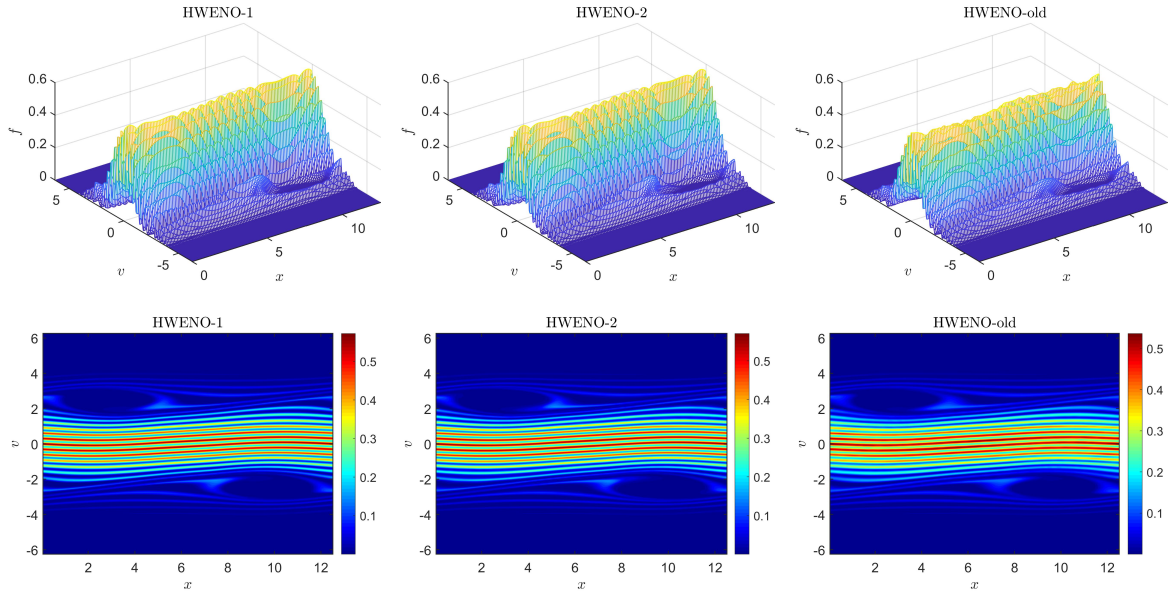


Figure 4.11: (Strong Landau damping). The mesh plots (top) and contour plots (bottom) of the numerical solutions of the SL HWENO-1 (left), HWENO-2 (middle), and HWENO-old (right) schemes at  $T = 40$ .

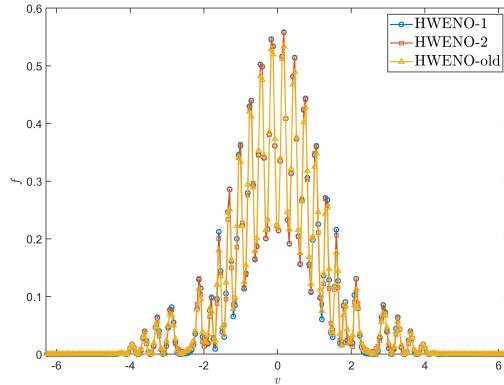


Figure 4.12: (Strong Landau damping). Cross-sections of the SL HWENO solutions at  $T = 40$  and at  $x = 2\pi$ .

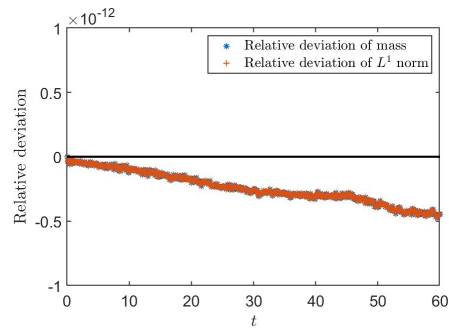


Figure 4.13: (Strong Landau damping). Performance of mass conservation and PP properties of the SL HWENO-1 scheme for the strong Landau damping with  $v_{\max} = 10$ .

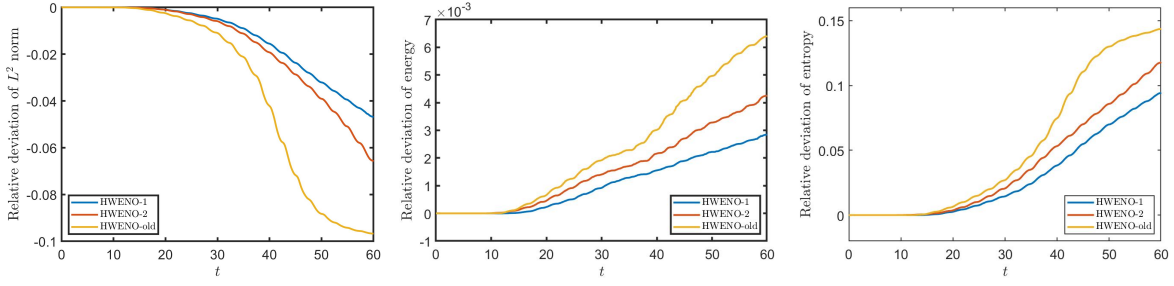


Figure 4.14: (Strong Landau damping). Relative deviations of the  $L^2$  norm (left), energy (middle), and entropy (right).

initial condition

$$f(x, v, t = 0) = \left( n_p \exp\left(-\frac{v^2}{2}\right) + n_b \exp\left(-\frac{(v-u)^2}{2v_t^2}\right) \right) (1 + 0.04 \cos(kx)), \quad (4.5)$$

$$x \in \left[0, \frac{20}{3}\pi\right], \quad v \in [-13, 13],$$

where  $n_p = \frac{9}{10\sqrt{2\pi}}$ ,  $n_b = \frac{2}{10\sqrt{2\pi}}$ ,  $u = 4.5$ ,  $v_t = 0.5$  and  $k = 0.3$ . In Figure 4.15, the mesh plots and contour plots of the numerical solutions of the SL HWENO schemes at  $T = 40$  are presented. The results are consistent with the existing ones in [5].

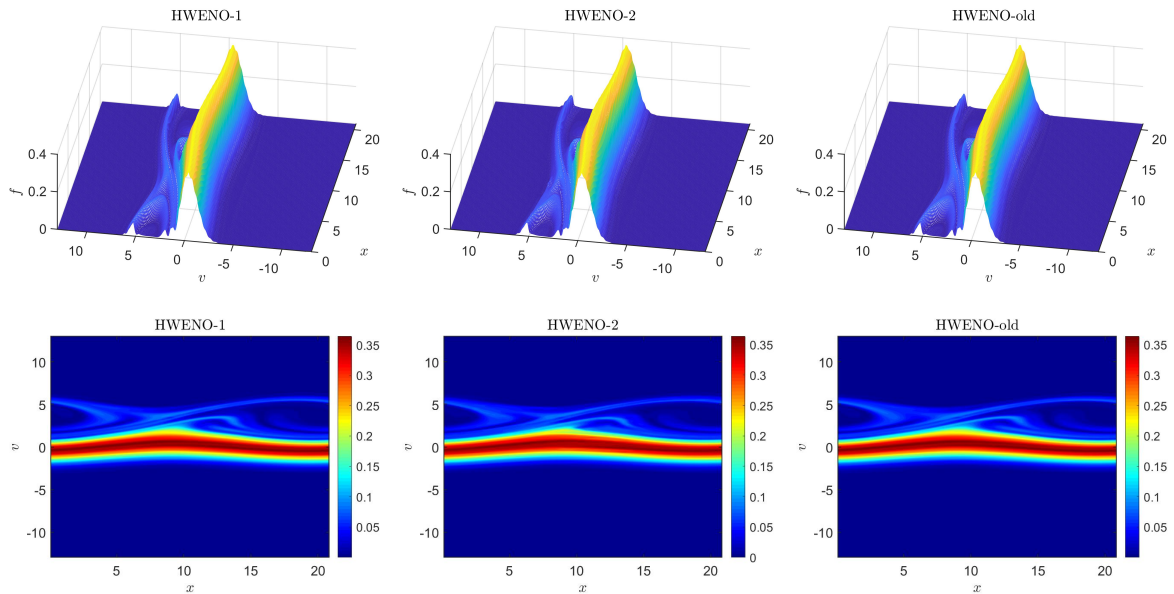


Figure 4.15: (Bump-on-tail instability). The mesh plots (top) and contour plots (bottom) of the numerical solutions of the SL HWENO-1 (left), HWENO-2 (middle), and HWENO-old (right) schemes at  $T = 40$ .

### 4.3. Guiding center Vlasov model

For the guiding center Vlasov model, unless specified, we set  $N_x = N_y = 256$ ,  $\text{CFL} = 10.2$ , and

$$\Delta t = \text{CFL} / (\max\{|E_1|\}/\Delta x + \max\{|E_2|\}/\Delta y).$$

**Example 4.5.** (Kelvin-Helmholtz instability problem). Consider the guiding center Vlasov model with the periodic boundary condition and with the following initial condition

$$\rho(x, y, 0) = \sin(y) + 0.015\cos(kx), \quad x \in [0, 4\pi], \quad y \in [0, 2\pi], \quad (4.6)$$

where  $k = 0.5$ . In Table 4.4, we show the  $L^2$  errors and corresponding orders of accuracy of the SL HWENO schemes at  $T = 5$ . The reference solutions are computed in the same way for the strong Landau damping. The SL HWENO schemes have similar results and the orders of accuracy are fourth. In Figure 4.16, we verify the fourth-order temporal accuracy for this problem. In Figure 4.17, we show the mesh plots and contour plots of the numerical solutions of the SL HWENO schemes at  $T = 40$ . The numerical results are comparable to the existing ones in the literature [36, 4]. We also provide the cross-sections of the numerical solutions of the SL HWENO schemes at  $y = \pi$  with the same settings as in Figure 4.17. As shown, the SL HWENO-1, and HWENO-2 schemes have better resolution than the SL HWENO-old scheme. However, the SL HWENO-1 scheme has distinct upward and downward overshooting comparing with the other two.

The guiding center Vlasov model conserves many quantities including mass, energy, and enstrophy [36, 4]. Similar to the strong Landau damping, we observe a  $O(10^{-12})$  level of deviation of mass for this problem. We omit this result for conciseness. For energy and enstrophy, we provide the relative deviations of them for the SL HWENO schemes in Figure 4.19. The performance for all the schemes are comparable to the existing results in the literature [36, 4].

Table 4.4: (Kelvin-Helmholtz instability problem).  $L^2$  errors and corresponding orders of accuracy of the SL HWENO schemes at  $T = 5$ .

mesh	HWENO-1		HWENO-2		HWENO-old	
	$L^2$ error	order	$L^2$ error	order	$L^2$ error	order
$16 \times 16$	2.27E-02	—	2.27E-02	—	2.28E-02	—
$32 \times 32$	5.08E-03	2.16	5.08E-03	2.16	5.08E-03	2.17
$64 \times 64$	6.54E-04	2.96	6.54E-04	2.96	6.54E-04	2.96
$128 \times 128$	5.78E-05	3.50	5.78E-05	3.50	5.78E-05	3.50
$256 \times 256$	4.42E-06	3.71	4.42E-06	3.71	4.42E-06	3.71



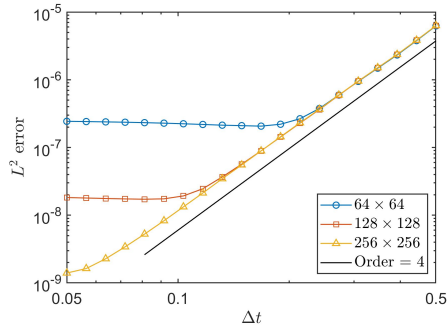


Figure 4.16: (Kelvin-Helmholtz instability problem). Temporal order of accuracy of the SL HWENO-1 scheme. The three colored lines use different mesh of  $64 \times 64$ ,  $128 \times 128$ , and  $256 \times 256$ . The programs stop at  $T = 5$ .

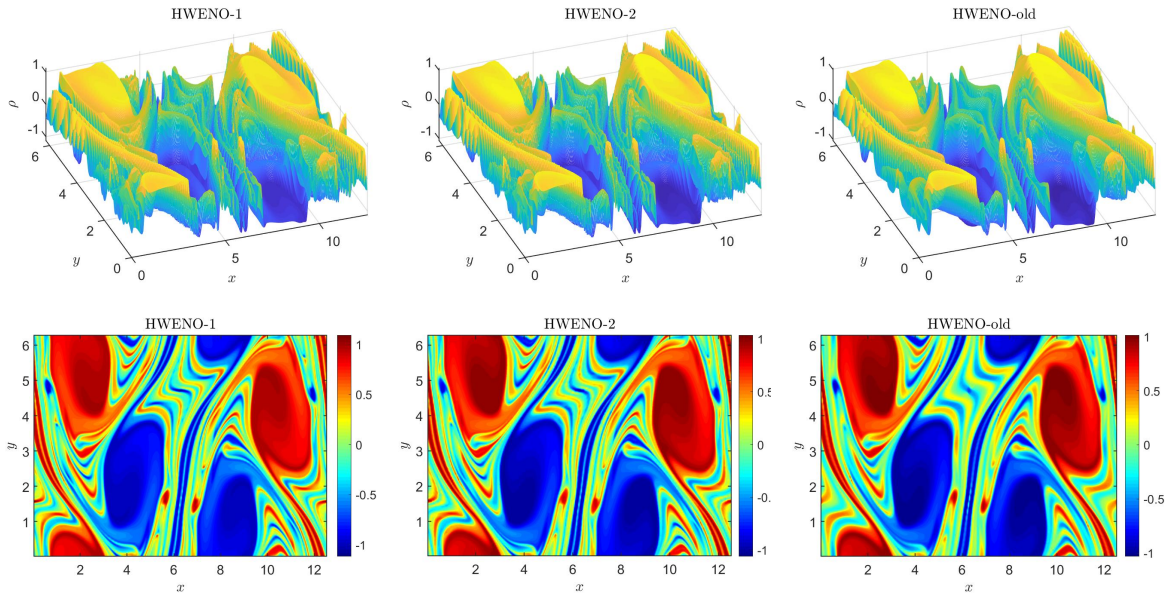


Figure 4.17: (Kelvin-Helmholtz instability problem). The mesh plots (left) and contour plots of the numerical solutions of the SL HWENO-1 (left), HWENO-2 (middle), and HWENO-old (right) schemes at  $T = 40$ .

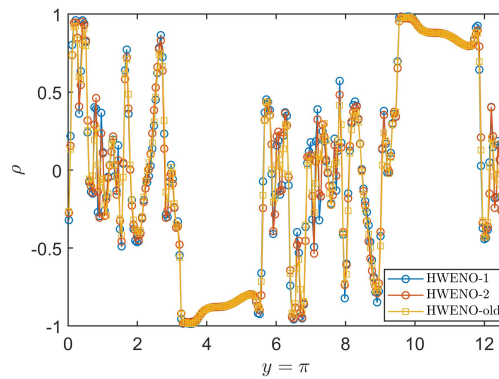


Figure 4.18: (Kelvin-Helmholtz instability problem). Cross-sections of SL HWENO solutions at  $T = 40$  and at  $y = \pi$ .

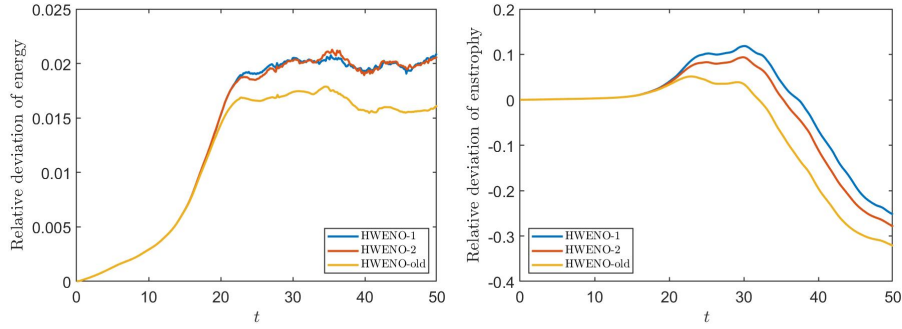


Figure 4.19: (Kelvin-Helmholtz instability problem). Relative deviations of energy (left) and enstrophy (right).

#### 4.4. Incompressible Euler equation

For the incompressible Euler equation, unless specified, we set  $N_x = N_y = 256$ ,  $\text{CFL} = 10.2$ , and

$$\Delta t = \text{CFL} / (\max\{u_1\} / \Delta x + \max\{u_2\} / \Delta y).$$

**Example 4.6.** (Shear flow problem). Consider the incompressible Euler equations in the domain  $[0, 2\pi] \times [0, 2\pi]$  with the following initial condition

$$\omega(x, y, 0) = \begin{cases} \delta \cos(x) - \frac{1}{\rho} \text{sech}^2\left(\frac{y-\pi/2}{\rho}\right), & \text{if } y \leq \pi, \\ \delta \cos(x) + \frac{1}{\rho} \text{sech}^2\left(\frac{3\pi/2-y}{\rho}\right), & \text{if } y > \pi, \end{cases} \quad (4.7)$$

where  $\delta = 0.05$  and  $\rho = \pi/15$ , and the periodic boundary condition. In Figure 4.20, we show the mesh plots and contour plots of the numerical solutions of the SL HWENO schemes at  $T = 8$ . In Figure 4.21, the cross-sections of the numerical solutions of the SL HWENO schemes at  $T = 8$  at  $x = \pi$  are provided. The three schemes performs similarly for this problem.

The incompressible Euler equation in vorticity-stream function formulation conserves mass, energy, and enstrophy [36, 4]. We observe a  $O(10^{-12})$  level of deviation of mass. We skip this result for conciseness. In Figure 4.22, we give the time history of relative deviations of energy and enstrophy of the SL HWENO schemes. The results are comparable to the existing ones [36, 4].

## 5. Conclusion

In this paper, we present new fourth-order SL HWENO schemes without operator splitting. Two new HWENO reconstruction methods are introduced for capturing complicated solution structures without excessive dissipation. The proposed schemes couple the weak formulation of the characteristic Galerkin method with the new HWENO reconstruction methods; the obtained SL HWENO

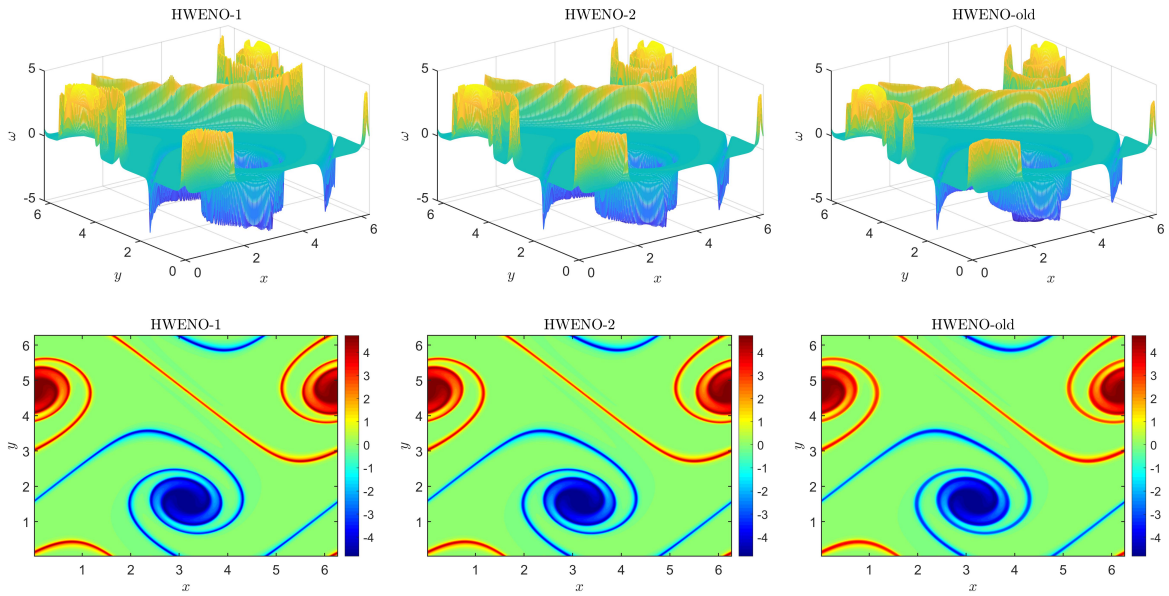


Figure 4.20: (Shear flow problem). The mesh plots (left) and contour plots of the numerical solutions of the SL HWENO-1 (left), HWENO-2 (middle), and HWENO-old (right) schemes at  $T = 8$ .

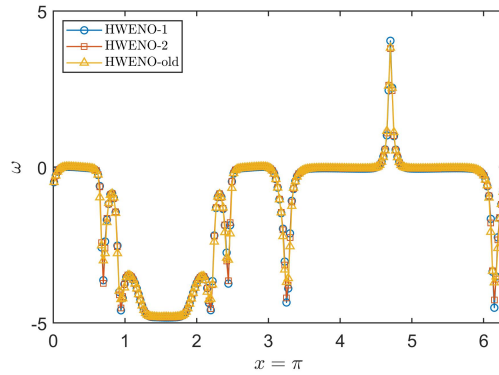


Figure 4.21: (Shear flow problem). Cross-sections of the SL HWENO solutions at  $T = 8$  and at  $x = \pi$ .

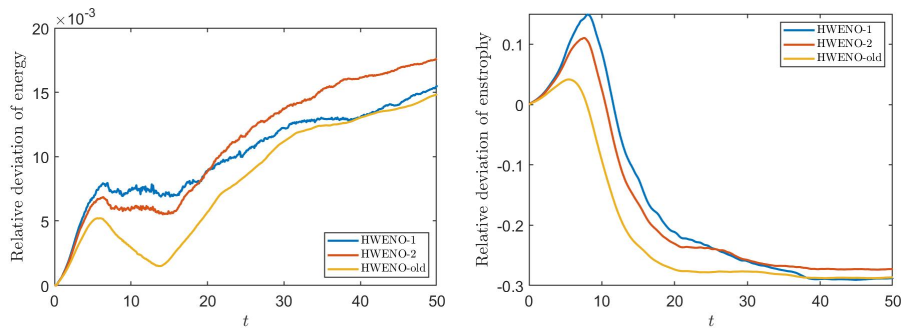


Figure 4.22: (Shear flow problem). Relative deviations of energy (left) and enstrophy (right).

schemes are fourth-order accurate in both space and time, mass conservative, PP, and unconditionally stable under a linearized setting. Good numerical performance is observed through a variety of tests.

## 6. Acknowledgements

The work of the first and fourth authors was partially supported by National Natural Science Foundation (China) [Grant Number 12071392]. The work of the second author was partially support by the Foundation of Beijing Normal University [Grant Numbers 28704-310432105], UIC Research Grant with No. of UICR0700035-22 at BNU-HKBU United International College, Zhuhai, PR China, Guangdong Higher Education Upgrading Plan (2021-2025) of "Rushing to the Top, Making Up Shortcomings and Strengthening Special Features" with No. of UICR0400024-21. The work of the third author was partially support by NSF [Grant Numbers NSF-DMS-1818924 and NSF-DMS-2111253], Air Force Office of Scientific Research, United States FA9550-18-1-0257.

# Appendices

## A. Coefficients of $\{q_k(x, y)\}_{k=0}^4$

For  $q_0(x, y)$ ,

$$\begin{aligned}
a_1^{q_0} &= \bar{u}_{i,j}, & a_2^{q_0} &= 12\widetilde{v}_{i,j}^n, & a_3^{q_0} &= 12\widetilde{w}_{i,j}^n, \\
a_4^{q_0} &= \frac{1}{2}\bar{u}_{i-1,j}^n - \bar{u}_{i,j}^n + \frac{1}{2}\bar{u}_{i+1,j}^n, \\
a_5^{q_0} &= \frac{1}{4}\bar{u}_{i-1,j-1}^n - \frac{1}{4}\bar{u}_{i+1,j-1}^n - \frac{1}{4}\bar{u}_{i-1,j+1}^n + \frac{1}{4}\bar{u}_{i+1,j+1}^n, \\
a_6^{q_0} &= \frac{1}{2}\bar{u}_{i,j-1}^n - \bar{u}_{i,j}^n + \frac{1}{2}\bar{u}_{i,j+1}^n, \\
a_7^{q_0} &= -\frac{5}{11}\bar{u}_{i-1,j}^n + \frac{5}{11}\bar{u}_{i+1,j}^n - \frac{120}{11}\widetilde{v}_{i,j}^n, \\
a_8^{q_0} &= -\frac{1}{4}\bar{u}_{i-1,j-1}^n + \frac{1}{2}\bar{u}_{i,j-1}^n - \frac{1}{4}\bar{u}_{i+1,j-1}^n + \frac{1}{4}\bar{u}_{i-1,j+1}^n - \frac{1}{2}\bar{u}_{i,j+1}^n + \frac{1}{4}\bar{u}_{i+1,j+1}^n, \\
a_9^{q_0} &= -\frac{1}{4}\bar{u}_{i-1,j-1}^n + \frac{1}{2}\bar{u}_{i-1,j}^n - \frac{1}{4}\bar{u}_{i-1,j+1}^n + \frac{1}{4}\bar{u}_{i+1,j-1}^n - \frac{1}{2}\bar{u}_{i+1,j}^n + \frac{1}{4}\bar{u}_{i+1,j+1}^n, \\
a_{10}^{q_0} &= -\frac{5}{11}\bar{u}_{i,j-1}^n + \frac{5}{11}\bar{u}_{i,j+1}^n - \frac{120}{11}\widetilde{w}_{i,j}^n.
\end{aligned} \tag{A.1}$$

For  $q_1(x, y)$ ,

$$\begin{aligned}
a_1^{q_1} &= \bar{u}_{i,j}^n, & a_2^{q_1} &= 12\widetilde{v}_{i,j}^n, & a_3^{q_1} &= 12\widetilde{w}_{i,j}^n, \\
a_4^{q_1} &= \bar{u}_{i-1,j}^n - \bar{u}_{i,j}^n + 12\widetilde{v}_{i,j}^n, \\
a_5^{q_1} &= \bar{u}_{i-1,j-1}^n - \bar{u}_{i,j-1}^n - \bar{u}_{i-1,j}^n + \bar{u}_{i,j}^n, \\
a_6^{q_1} &= \bar{u}_{i,j-1}^n - \bar{u}_{i,j}^n + 12\widetilde{w}_{i,j}^n.
\end{aligned} \tag{A.2}$$

For  $q_2(x, y)$ ,

$$\begin{aligned}
a_1^{q_2} &= \bar{u}_{i,j}^n, & a_2^{q_2} &= 12\widetilde{v}_{i,j}^n, & a_3^{q_2} &= 12\widetilde{w}_{i,j}^n, \\
a_4^{q_2} &= -\bar{u}_{i,j}^n + \bar{u}_{i+1,j}^n - 12\widetilde{v}_{i,j}^n, \\
a_5^{q_2} &= \bar{u}_{i,j-1}^n - \bar{u}_{i+1,j-1}^n - \bar{u}_{i,j}^n + \bar{u}_{i+1,j}^n, \\
a_6^{q_2} &= \bar{u}_{i,j-1}^n - \bar{u}_{i,j}^n + 12\widetilde{w}_{i,j}^n.
\end{aligned} \tag{A.3}$$

For  $q_3(x, y)$ ,

$$\begin{aligned}
a_1^{q_3} &= \bar{u}_{i,j}^n, & a_2^{q_3} &= 12\widetilde{v}_{i,j}^n, & a_3^{q_3} &= 12\widetilde{w}_{i,j}^n, \\
a_4^{q_3} &= \bar{u}_{i-1,j}^n - \bar{u}_{i,j}^n + 12\widetilde{v}_{i,j}^n, \\
a_5^{q_3} &= \bar{u}_{i-1,j}^n - \bar{u}_{i,j}^n - \bar{u}_{i-1,j+1}^n + \bar{u}_{i,j+1}^n, \\
a_6^{q_3} &= -\bar{u}_{i,j}^n + \bar{u}_{i,j+1}^n - 12\widetilde{w}_{i,j}^n.
\end{aligned} \tag{A.4}$$

For  $q_4(x, y)$ ,

$$\begin{aligned}
a_1^{q_4} &= \bar{u}_{i,j}^n, & a_2^{q_4} &= 12\widetilde{v}_{i,j}^n, & a_3^{q_4} &= 12\widetilde{w}_{i,j}^n, \\
a_4^{q_4} &= -\bar{u}_{i,j}^n + \bar{u}_{i+1,j}^n - 12\widetilde{v}_{i,j}^n, \\
a_5^{q_4} &= \bar{u}_{i,j}^n - \bar{u}_{i+1,j}^n - \bar{u}_{i,j+1}^n + \bar{u}_{i+1,j+1}^n, \\
a_6^{q_4} &= -\bar{u}_{i,j}^n + \bar{u}_{i,j+1}^n - 12\widetilde{w}_{i,j}^n.
\end{aligned} \tag{A.5}$$

## B. Numerical proof of Remark 2.1

Consider the following linear transport equation,

$$u_t + au_x + bu_y = 0 \tag{B.1}$$

with periodic boundary condition. Without loss of generality, we assume that  $a > 0$  and  $b > 0$ . We define  $\theta_1 = \frac{a\Delta t}{\Delta x}$  and  $\theta_2 = \frac{b\Delta t}{\Delta y}$ . Then (2.35) with  $H^n(x, y)$  reconstructed by the linear reconstruction

is reorganized as follows:

$$\begin{aligned}
\bar{u}_{i,j}^{n+1} &= \frac{1}{\Delta x \Delta y} \left[ \int_{x_{i-\frac{1}{2}}-\theta_1 \Delta x}^{x_{i-\frac{1}{2}}-[\theta_1] \Delta x} \int_{y_{j-\frac{1}{2}}-\theta_2 \Delta y}^{y_{j-\frac{1}{2}}-[\theta_2] \Delta y} H^{(i-1-[\theta_1], j-1-[\theta_2])}(x, y) dx dy \right. \\
&\quad + \int_{x_{i-\frac{1}{2}}-[\theta_1] \Delta x}^{x_{i-\frac{1}{2}}+(1-\theta_1) \Delta x} \int_{y_{j-\frac{1}{2}}-\theta_2 \Delta y}^{y_{j-\frac{1}{2}}-[\theta_2] \Delta y} H^{(i-[\theta_1], j-1-[\theta_2])}(x, y) dx dy \\
&\quad + \int_{x_{i-\frac{1}{2}}-\theta_1 \Delta x}^{x_{i-\frac{1}{2}}-[\theta_1] \Delta x} \int_{y_{j-\frac{1}{2}}-[\theta_2] \Delta y}^{y_{j-\frac{1}{2}}+(1-\theta_2) \Delta y} H^{(i-1-[\theta_1], j-[\theta_2])}(x, y) dx dy \\
&\quad \left. + \int_{x_{i-\frac{1}{2}}-[\theta_1] \Delta x}^{x_{i-\frac{1}{2}}+(1-\theta_1) \Delta x} \int_{y_{j-\frac{1}{2}}-[\theta_2] \Delta y}^{y_{j-\frac{1}{2}}+(1-\theta_2) \Delta y} H^{(i-[\theta_1], j-[\theta_2])}(x, y) dx dy, \right. \tag{B.2}
\end{aligned}$$

$$\begin{aligned}
\bar{v}_{i,j}^{n+1} &= \frac{1}{\Delta x \Delta y} \left[ \int_{x_{i-\frac{1}{2}}-\theta_1 \Delta x}^{x_{i-\frac{1}{2}}-[\theta_1] \Delta x} \int_{y_{j-\frac{1}{2}}-\theta_2 \Delta y}^{y_{j-\frac{1}{2}}-[\theta_2] \Delta y} H^{(i-1-[\theta_1], j-1-[\theta_2])}(x, y) \left( \frac{x + \theta_1 \Delta x - x_i}{\Delta x} \right) dx dy \right. \\
&\quad + \int_{x_{i-\frac{1}{2}}-[\theta_1] \Delta x}^{x_{i-\frac{1}{2}}+(1-\theta_1) \Delta x} \int_{y_{j-\frac{1}{2}}-\theta_2 \Delta y}^{y_{j-\frac{1}{2}}-[\theta_2] \Delta y} H^{(i-[\theta_1], j-1-[\theta_2])}(x, y) \left( \frac{x + \theta_1 \Delta x - x_i}{\Delta x} \right) dx dy \\
&\quad + \int_{x_{i-\frac{1}{2}}-\theta_1 \Delta x}^{x_{i-\frac{1}{2}}-[\theta_1] \Delta x} \int_{y_{j-\frac{1}{2}}-[\theta_2] \Delta y}^{y_{j-\frac{1}{2}}+(1-\theta_2) \Delta y} H^{(i-1-[\theta_1], j-[\theta_2])}(x, y) \left( \frac{x + \theta_1 \Delta x - x_i}{\Delta x} \right) dx dy \\
&\quad \left. + \int_{x_{i-\frac{1}{2}}-[\theta_1] \Delta x}^{x_{i-\frac{1}{2}}+(1-\theta_1) \Delta x} \int_{y_{j-\frac{1}{2}}-[\theta_2] \Delta y}^{y_{j-\frac{1}{2}}+(1-\theta_2) \Delta y} H^{(i-[\theta_1], j-[\theta_2])}(x, y) \left( \frac{x + \theta_1 \Delta x - x_i}{\Delta x} \right) dx dy, \right. \tag{B.3}
\end{aligned}$$

and

$$\begin{aligned}
\bar{w}_{i,j}^{n+1} &= \frac{1}{\Delta x \Delta y} \left[ \int_{x_{i-\frac{1}{2}}-\theta_1 \Delta x}^{x_{i-\frac{1}{2}}-[\theta_1] \Delta x} \int_{y_{j-\frac{1}{2}}-\theta_2 \Delta y}^{y_{j-\frac{1}{2}}-[\theta_2] \Delta y} H^{(i-1-[\theta_1], j-1-[\theta_2])}(x, y) \left( \frac{y + \theta_2 \Delta y - y_j}{\Delta y} \right) dx dy \right. \\
&\quad + \int_{x_{i-\frac{1}{2}}-[\theta_1] \Delta x}^{x_{i-\frac{1}{2}}+(1-\theta_1) \Delta x} \int_{y_{j-\frac{1}{2}}-\theta_2 \Delta y}^{y_{j-\frac{1}{2}}-[\theta_2] \Delta y} H^{(i-[\theta_1], j-1-[\theta_2])}(x, y) \left( \frac{y + \theta_2 \Delta y - y_j}{\Delta y} \right) dx dy \\
&\quad + \int_{x_{i-\frac{1}{2}}-\theta_1 \Delta x}^{x_{i-\frac{1}{2}}-[\theta_1] \Delta x} \int_{y_{j-\frac{1}{2}}-[\theta_2] \Delta y}^{y_{j-\frac{1}{2}}+(1-\theta_2) \Delta y} H^{(i-1-[\theta_1], j-[\theta_2])}(x, y) \left( \frac{y + \theta_2 \Delta y - y_j}{\Delta y} \right) dx dy \\
&\quad \left. + \int_{x_{i-\frac{1}{2}}-[\theta_1] \Delta x}^{x_{i-\frac{1}{2}}+(1-\theta_1) \Delta x} \int_{y_{j-\frac{1}{2}}-[\theta_2] \Delta y}^{y_{j-\frac{1}{2}}+(1-\theta_2) \Delta y} H^{(i-[\theta_1], j-[\theta_2])}(x, y) \left( \frac{y + \theta_2 \Delta y - y_j}{\Delta y} \right) dx dy, \right. \tag{B.4}
\end{aligned}$$

where  $[\cdot]$  represents the largest integer smaller than the input number. Now, we assume that

$$\bar{u}_{p,q}^n = \bar{u}^n e^{I \xi_1 p \Delta x} e^{I \xi_2 q \Delta y}, \quad \bar{v}_{p,q}^n = \bar{v}^n e^{I \xi_1 p \Delta x} e^{I \xi_2 q \Delta y}, \quad \bar{w}_{p,q}^n = \bar{w}^n e^{I \xi_1 p \Delta x} e^{I \xi_2 q \Delta y} \quad \forall p, q, \tag{B.5}$$

and

$$\bar{u}_{i,j}^{n+1} = \bar{u}^{n+1} e^{I \xi_1 i \Delta x} e^{I \xi_2 j \Delta y}, \quad \bar{v}_{i,j}^{n+1} = \bar{v}^{n+1} e^{I \xi_1 i \Delta x} e^{I \xi_2 j \Delta y}, \quad \bar{w}_{i,j}^{n+1} = \bar{w}^{n+1} e^{I \xi_1 i \Delta x} e^{I \xi_2 j \Delta y}, \tag{B.6}$$

where  $I = \sqrt{-1}$ . Submitting (B.5) and (B.6) into (B.2)-(B.4), we find that

$$\begin{bmatrix} \bar{u}^{n+1} \\ \bar{v}^{n+1} \\ \bar{w}^{n+1} \end{bmatrix} = A(\theta_1, \theta_2, \xi_1, \xi_2) \begin{bmatrix} \bar{u}^n \\ \bar{v}^n \\ \bar{w}^n \end{bmatrix}, \quad (\text{B.7})$$

where  $A(\theta_1, \theta_2, \xi_1, \xi_2)$  is the  $3 \times 3$  amplification matrix. We skip the explicit expression of  $A(\theta_1, \theta_2, \xi_1, \xi_2)$  for conciseness since it is very complicated. We denote the spectral radius of  $A(\theta_1, \theta_2, \xi_1, \xi_2)$  by  $\rho(A(\theta_1, \theta_2, \xi_1, \xi_2))$ . With basic algebraic manipulation, we have

$$A(\theta_1, \theta_2, \xi_1, \xi_2) = e^{-I\xi_1 \lfloor \theta_1 \rfloor \Delta x} e^{-I\xi_2 \lfloor \theta_2 \rfloor \Delta y} A(\theta_1 - \lfloor \theta_1 \rfloor, \theta_2 - \lfloor \theta_2 \rfloor, \xi_1, \xi_2). \quad (\text{B.8})$$

Hence, by von Nuemann analysis, it is sufficient to verify that  $\rho(A(\theta_1, \theta_2, \xi_1, \xi_2)) \leq 1$  for any  $\theta_1, \theta_2 \in [0, 1]$  and  $\xi_1 \Delta x, \xi_2 \Delta y \in [0, 2\pi]$ . It is impossible to provide the theoretical expression of  $\rho(A(\theta_1, \theta_2, \xi_1, \xi_2))$ . We numerically verify this relation by sampling 1000 uniform points over each  $\theta_1, \theta_2, \xi_1 \Delta x, \xi_2 \Delta y$  domain. We find that all the  $\rho(A(\cdot, \cdot, \cdot, \cdot))$  values computed by the sampling points are not greater than 1, which validates Remark 2.1.

## References

- [1] T. Arber and R. Vann. A Critical Comparison of Eulerian-Grid-Based Vlasov Solvers. *Journal of Computational Physics*, 180(1):339–357, 2002.
- [2] R. Borges, M. Carmona, B. Costa, and W. S. Don. An improved weighted essentially non-oscillatory scheme for hyperbolic conservation laws. *Journal of Computational Physics*, 227(6):3191–3211, 2008.
- [3] P. A. Bosler, A. M. Bradley, and M. A. Taylor. Conservative Multimoment Transport along Characteristics for Discontinuous Galerkin Methods. *SIAM Journal on Scientific Computing*, 41(4):B870–B902, 2019.
- [4] X. Cai, S. Boscarino, and J.-M. Qiu. High order semi-lagrangian discontinuous Galerkin method coupled with Runge-Kutta exponential integrators for nonlinear Vlasov dynamics. *Journal of Computational Physics*, 427:110036, 2021.
- [5] X. Cai, W. Guo, and J.-M. Qiu. A high order semi-Lagrangian discontinuous Galerkin method for Vlasov–Poisson simulations without operator splitting. *Journal of Computational Physics*, 354:529–551, 2018.

- [6] X. Cai, J. Qiu, and J.-M. Qiu. A conservative semi-Lagrangian HWENO method for the Vlasov equation. *Journal of Computational Physics*, 323:95–114, 2016.
- [7] X. Cai, X. Zhang, and J. Qiu. Positivity-preserving high order finite volume HWENO schemes for compressible Euler equations. *Journal of Scientific Computing*, 68(2):464–483, 2016.
- [8] E. Celledoni, A. Marthinsen, and B. Owren. Commutator-free Lie group methods. *Future Generation Computer Systems*, 19(3):341–352, 2003.
- [9] N. Crouseilles, M. Mehrenberger, and E. Sonnendrücker. Conservative semi-Lagrangian schemes for Vlasov equations. *Journal of Computational Physics*, 229(6):1927–1953, 2010.
- [10] H. K. Dahle, R. E. Ewing, and T. F. Russell. Eulerian-Lagrangian localized adjoint methods for a nonlinear advection-diffusion equation. *Computer methods in applied mechanics and engineering*, 122(3-4):223–250, 1995.
- [11] Z. Du and J. Li. A Hermite WENO reconstruction for fourth order temporal accurate schemes based on the GRP solver for hyperbolic conservation laws. *Journal of Computational Physics*, 355:385–396, 2018.
- [12] M. Dumbser, D. S. Balsara, E. F. Toro, and C.-D. Munz. A unified framework for the construction of one-step finite volume and discontinuous Galerkin schemes on unstructured meshes. *Journal of Computational Physics*, 227(18):8209–8253, 2008.
- [13] F. Filbet, E. Sonnendrücker, and P. Bertrand. Conservative Numerical Schemes for the Vlasov Equation. *Journal of Computational Physics*, 172(1):166–187, 2001.
- [14] E. Frénod, S. A. Hirstoaga, M. Lutz, and E. Sonnendrücker. Long Time Behaviour of an Exponential Integrator for a Vlasov-Poisson System with Strong Magnetic Field. *Communications in Computational Physics*, 18(2):263–296, 2015.
- [15] L. Fu. A very-high-order TENO scheme for all-speed gas dynamics and turbulence. *Computer Physics Communications*, 244:117–131, 2019.
- [16] L. Fu, X. Y. Hu, and N. A. Adams. A family of high-order targeted ENO schemes for compressible-fluid simulations. *Journal of Computational Physics*, 305:333–359, 2016.



- [17] L. Fu, X. Y. Hu, and N. A. Adams. A new class of adaptive high-order targeted eno schemes for hyperbolic conservation laws. *Journal of Computational Physics*, 374:724–751, 2018.
- [18] W. Guo, R. D. Nair, and J. M. Qiu. A Conservative Semi-Lagrangian Discontinuous Galerkin Scheme on the Cubed-Sphere. *Monthly Weather Review*, 142(1):457–475, 2014.
- [19] C.-S. Huang, T. Arbogast, and C.-H. Hung. A semi-Lagrangian finite difference WENO scheme for scalar nonlinear conservation laws. *Journal of Computational Physics*, 322:559–585, 2016.
- [20] W. Indra, Yanuar, and K. Engkos, A. Fifth-Order Hermite Targeted Essentially Non-oscillatory Schemes for Hyperbolic Conservation Laws. *Journal of Scientific Computing*, 87:69, 2021.
- [21] G.-S. Jiang and C.-W. Shu. Efficient implementation of weighted ENO schemes. *Journal of Computational Physics*, 126(1):202–228, 1996.
- [22] D. Lee, R. B. Lowrie, M. R. Petersen, T. D. Ringler, and M. W. Hecht. A high order characteristic discontinuous Galerkin scheme for advection on unstructured meshes. *Journal of Computational Physics*, 324:289–302, 2016.
- [23] X.-D. Liu, S. Osher, and T. Chan. Weighted essentially non-oscillatory schemes. *Journal of Computational Physics*, 115(1):200–212, 1994.
- [24] K. W. Morton. On the Analysis of Finite Volume Methods for Evolutionary Problems. *SIAM Journal on Numerical Analysis*, 35(6):2195–2222, 1998.
- [25] O. Pironneau. A semi-Lagrangian high-order method for Navier-Stokes equations. *Numerische Mathematik*, 38:309–332, 1982.
- [26] J. Qiu and C.-W. Shu. Hermite WENO schemes and their application as limiters for Runge–Kutta discontinuous Galerkin method: one-dimensional case. *Journal of Computational Physics*, 193(1):115–135, 2004.
- [27] J. Qiu and C.-W. Shu. Hermite WENO schemes and their application as limiters for Runge–Kutta discontinuous Galerkin method II: Two dimensional case. *Computers & Fluids*, 34(6):642–663, 2005.

- [28] J.-M. Qiu and C.-W. Shu. Conservative high order semi-Lagrangian finite difference WENO methods for advection in incompressible flow. *Journal of Computational Physics*, 230(4):863–889, 2011.
- [29] J.-M. Qiu and C.-W. Shu. Positivity preserving semi-Lagrangian discontinuous Galerkin formulation: Theoretical analysis and application to the Vlasov–Poisson system. *Journal of Computational Physics*, 230(23):8386–8409, 2011.
- [30] M. Restelli, L. Bonaventura, and R. Sacco. A semi-Lagrangian discontinuous Galerkin method for scalar advection by incompressible flows. *Journal of Computational Physics*, 216(1):195–215, 2006.
- [31] J. A. Rossmannith and D. C. Seal. A positivity-preserving high-order semi-Lagrangian discontinuous Galerkin scheme for the Vlasov–Poisson equations. *Journal of Computational Physics*, 230(16):6203–6232, 2011.
- [32] T. F. Russell and M. A. Celia. An overview of research on Eulerian-Lagrangian localized adjoint methods (ELLAM). *Advances in Water Resources*, 25(8-12):1215–1231, 2002.
- [33] C.-W. Shu. Essentially non-oscillatory and weighted essentially non-oscillatory schemes for hyperbolic conservation laws. In *Advanced numerical approximation of nonlinear hyperbolic equations*, pages 325–432. Springer, 1998.
- [34] D. Sirajuddin and W. N. Hitchon. A truly forward semi-Lagrangian WENO scheme for the Vlasov-Poisson system. *Journal of Computational Physics*, 392:619–665, 2019.
- [35] A. Staniforth and J. Côté. Semi-Lagrangian integration schemes for atmospheric models—a review. *Journal of Computational Physics*, 119:2206–2223, 1991.
- [36] T. Xiong, G. Russo, and J. Qiu. Conservative Multi-dimensional Semi-Lagrangian Finite Difference Scheme: Stability and Applications to the Kinetic and Fluid Simulations. *Journal of Scientific Computing*, 79:1241–1270, 2019.
- [37] D. Xiu and G. E. Karniadakis. A Semi-Lagrangian High-Order Method for Navier–Stokes Equations. *Journal of Computational Physics*, 172:658–684, 2001.

- [38] C. Yang and F. Filbet. Conservative and non-conservative methods based on Hermite weighted essentially non-oscillatory reconstruction for Vlasov equations. *Journal of Computational Physics*, 279:18–36, 2014.
- [39] X. Zhang and C.-W. Shu. On maximum-principle-satisfying high order schemes for scalar conservation laws. *Journal of Computational Physics*, 229(9):3091–3120, 2010.
- [40] Z. Zhao and J. Qiu. A Hermite WENO scheme with artificial linear weights for hyperbolic conservation laws. *Journal of Computational Physics*, 417:109583, 2020.
- [41] N. Zheng, X. Cai, J.-M. Qiu, and J. Qiu. A Conservative Semi-Lagrangian Hybrid Hermite WENO Scheme for Linear Transport Equations and the Nonlinear Vlasov–Poisson System. *SIAM Journal on Scientific Computing*, 43(5):A3580–A3606, 2021.
- [42] N. Zheng, X. Cai, J.-M. Qiu, and J. Qiu. A fourth-order conservative semi-Lagrangian finite volume WENO scheme without operator splitting for kinetic and fluid simulations. *Computer Methods in Applied Mechanics and Engineering*, 395:114973, 2022.
- [43] J. Zhu and J. Qiu. A new fifth order finite difference WENO scheme for solving hyperbolic conservation laws. *Journal of Computational Physics*, 318:110–121, 2016.